

PARTICLE ACCELERATION AND PLASMA DYNAMICS DURING MAGNETIC RECONNECTION IN THE MAGNETICALLY DOMINATED REGIME

FAN GUO¹, YI-HSIN LIU², WILLIAM DAUGHTON¹, AND HUI LI¹

¹ Los Alamos National Laboratory, Los Alamos, NM 87545, USA; guofan.ustc@gmail.com

² NASA Goddard Space Flight Center, Greenbelt, MD 20771, USA

Received 2015 February 12; accepted 2015 April 28; published 2015 June 17

ABSTRACT

Magnetic reconnection is thought to be the driver for many explosive phenomena in the universe. The energy release and particle acceleration during reconnection have been proposed as a mechanism for producing high-energy emissions and cosmic rays. We carry out two- and three-dimensional (3D) kinetic simulations to investigate relativistic magnetic reconnection and the associated particle acceleration. The simulations focus on electron–positron plasmas starting with a magnetically dominated, force-free current sheet ($\sigma \equiv B^2/(4\pi n_e m_e c^2) \gg 1$). For this limit, we demonstrate that relativistic reconnection is highly efficient at accelerating particles through a first-order Fermi process accomplished by the curvature drift of particles along the electric field induced by the relativistic flows. This mechanism gives rise to the formation of hard power-law spectra $f \propto (\gamma - 1)^{-p}$ and approaches $p = 1$ for sufficiently large σ and system size. Eventually most of the available magnetic free energy is converted into nonthermal particle kinetic energy. An analytic model is presented to explain the key results and predict a general condition for the formation of power-law distributions. The development of reconnection in these regimes leads to relativistic inflow and outflow speeds and enhanced reconnection rates relative to nonrelativistic regimes. In the 3D simulation, the interplay between secondary kink and tearing instabilities leads to strong magnetic turbulence, but does not significantly change the energy conversion, reconnection rate, or particle acceleration. This study suggests that relativistic reconnection sites are strong sources of nonthermal particles, which may have important implications for a variety of high-energy astrophysical problems.

Key words: acceleration of particles – galaxies: jets – gamma-ray burst: general – magnetic reconnection – pulsars: general – relativistic processes

1. INTRODUCTION

Magnetic reconnection is a fundamental plasma process that rapidly rearranges magnetic topology and converts magnetic energy into various forms of plasma kinetic energy, including bulk plasma flow, thermal and nonthermal plasma distributions (Kulsrud 1998; Priest & Forbes 2000). It is thought to play an important role during explosive energy release processes of a wide variety of laboratory, space, and astrophysical systems including tokamak, planetary magnetospheres, solar flares, and high-energy astrophysical objects. Relativistic magnetic reconnection is often invoked to explain high-energy emissions and ultra-high-energy cosmic rays from objects such as pulsar wind nebulae (PWNe; Kirk 2004; Arons 2012; Uzdensky & Spitkovsky 2014), jets from active galactic nuclei (AGNs; de Gouveia dal Pino & Lazarian 2005; Giannios et al. 2009), and gamma-ray bursts (GRBs; Thompson 1994; Zhang & Yan 2011; McKinney & Uzdensky 2012). In those systems, the magnetization parameter $\sigma \equiv B^2/(4\pi n_e m_e c^2)$, is often estimated to be much larger than unity, $\sigma \gg 1$, and the Alfvén speed approaches the speed of light $v_A \sim c$. To explain the observed high-energy emissions, often an efficient energy conversion mechanism is required (e.g., Zhang et al. 2007, 2013; Celotti & Ghisellini 2008; Zhang & Yan 2011). Collisionless shocks, which can efficiently convert plasma flow energy into thermal and nonthermal energies in low- σ flows, are inefficient in dissipating magnetically dominated flows, where most of the energy is stored in magnetic fields. In these regimes, magnetic reconnection is the primary candidate for dissipating and converting magnetic energy into relativistic particles and subsequent radiation. Understanding magnetic reconnection is also

important for solving the so-called σ -problem (Coroniti 1990; Lyubarsky & Kirk 2001; Kirk & Skjæraasen 2003; Porth et al. 2013), where strong magnetic dissipation may be required to convert the magnetically dominated flow ($\sigma \gg 1$) to a matter-dominated flow ($\sigma \ll 1$). However, the detailed physics of relativistic magnetic reconnection, including the magnetic reconnection rate, energy conversion, and particle acceleration, are not well understood.

Blackman & Field (1994) and Lyutikov & Uzdensky (2003) have studied the properties of relativistic magnetic reconnection using the extended Sweet–Parker and Petschek models. They found that when $\sigma \gg 1$ the outflow speed u_{out} approaches the speed of light, and the rate of relativistic magnetic reconnection and inflow velocity u_{in} may increase compared to the nonrelativistic case. This is because of the enhanced outflow density arising from the Lorentz contraction of plasma passing through the diffusion region $u_{\text{in}} \propto u_{\text{out}} \Gamma_{\text{out}}/\Gamma_{\text{in}}$, where Γ_{out} and Γ_{in} are Lorentz factors of outflows and inflows, respectively. However, later analysis (Lyubarsky 2005) showed that for a pressure-balanced current layer ($B^2/8\pi \sim nk(T_i + T_e)$), the thermal pressure constrains the outflow speed to be mildly relativistic and hence the effect of Lorentz contraction is negligible. Although the rate of relativistic magnetic reconnection is reported to increase in a number of studies using different models (Zenitani et al. 2009; Bessho & Bhattacharjee 2012; Takamoto 2013; Comisso & Asenjo 2014; Guo et al. 2014; Melzani et al. 2014a; Sironi & Spitkovsky 2014), its nature is not clear. This issue has recently been revisited by carefully analyzing results from fully kinetic two-dimensional (2D) simulations (Liu et al. 2015), which show that the plasma density and pressure around the X-line

drop significantly as the initial high-pressure region is depleted during reconnection. This results in a reconnection region with $\sigma \gg 1$ and a relativistic inflow speed $v_{\text{in}} \sim c$. The local reconnection rate across the diffusion region is well predicted by a simple model that includes the Lorentz contraction. However, the extension of these results to three-dimensional (3D) kinetic simulations was not considered.

Plasma energization during magnetic reconnection has been extensively discussed in the literature. However, the primary acceleration mechanism is still unclear. Romanova & Lovelace (1992) analyzed particle motions in a large-scale reconnection region and predicted a spectrum $dN/d\gamma = \gamma^{-p}$ with $p = 1.5$ for the pair plasma case. Litvinenko (1999) found a solution with a spectral index $p = 2$ when particles are accelerated in a direct electric field associated with magnetic reconnection. Using a model for the motions of particles in a steady magnetic reconnection region, Larrabee et al. (2003) have found strong particle acceleration in the reconnection layer and obtained a hard energy spectrum with a spectral index of about $p = 1$. First-order Fermi acceleration in converging reconnection inflows has been proposed as a primary acceleration mechanism (de Gouveia dal Pino & Lazarian 2005; Lazarian & Opher 2009; Kowal et al. 2012). Drury (2012) studied the acceleration in a reconnection layer including energy change in both inflows and outflows and demonstrated that fluid compression is crucial for efficient particle acceleration. The test-particle approach has been applied to interpret the strong particle acceleration responsible for γ -ray flares from the Crab pulsar (Cerutti et al. 2012). The results suggest that magnetic reconnection may be responsible for producing the extreme particle acceleration required to explain high-energy emissions from the Crab flares (see also Cerutti et al. 2013). Self-consistent kinetic simulations have been widely used to study plasma dynamics and particle energization during magnetic reconnection. Most previous kinetic studies have focused on the regime with $\sigma \lesssim 1$, and found a number of acceleration mechanisms such as direct acceleration at X-line regions (Drake et al. 2005; Fu et al. 2006; Pritchett 2006; Huang et al. 2010; Oka et al. 2010) and Fermi-type acceleration in reconnection-induced plasma flows within magnetic islands (Drake et al. 2006, 2010; Huang et al. 2010; Oka et al. 2010). A recent attempt to incorporate different acceleration mechanisms into a new transport equation is presented by Zank et al. (2014). The high- σ regime ($\sigma > 1$) has been explored in a number of papers using the Harris equilibrium (Zenitani & Hoshino 2001, 2007; Liu et al. 2011; Bessho & Bhattacharjee 2012; Cerutti et al. 2013; Melzani et al. 2014b; Sironi & Spitkovsky 2014; Werner et al. 2014). However, the initial condition employed in these studies requires a hot plasma component inside the current sheet to maintain force balance, which may not be justified for high- σ plasmas. Recently, several studies have reported hard power-law distributions $1 \leq p \leq 2$ when $\sigma \gg 1$ (Guo et al. 2014; Melzani et al. 2014b; Sironi & Spitkovsky 2014; Werner et al. 2014). For a Harris current layer, it was found that a power-law distribution can be obtained by subtracting the initial hot plasma component in the current layer (Melzani et al. 2014b; Sironi & Spitkovsky 2014; Werner et al. 2014). In contrast, Guo et al. (2014) used a force-free current sheet that does not require the hot plasma population and showed that the energy distribution of particles within the entire reconnection layer develops a power-law distribution. In this study, the primary acceleration mechanism

was demonstrated to be a first-order Fermi mechanism resulting from the curvature drift of particles in the direction of the electric field induced by the relativistic flows. This mechanism gives rise to the formation of hard power-law spectra $f \propto (\gamma - 1)^{-p}$ with spectral index approaching $p = 1$ for a sufficiently high σ and a large system size. An analytical model was developed to describe the main feature of the simulations and it gives a general condition for the formation of the power-law particle energy distribution. The solution also appears to explain simulations from the Harris current layer, in which the particles initially in the current layer form a heated thermal distribution and particles injected from the upstream region are accelerated into a power-law distribution (Melzani et al. 2014b; Sironi & Spitkovsky 2014; Werner et al. 2014).

Another important issue is the influence of 3D dynamics that may significantly modify the reconnection rate, energy release, and particle acceleration process. Recently, the rate of 3D nonrelativistic magnetic reconnection has been explored and compared with 2D simulations in a number of nonrelativistic studies (Liu et al. 2013; Daughton et al. 2014), which showed only modest differences between 2D and 3D simulations although strong 3D effects emerge as the tearing mode develops over a range of oblique angles (Daughton et al. 2011). For relativistic magnetic reconnection with a pair plasma, Sironi & Spitkovsky (2014) reported a decrease of reconnection rate by a factor of 4 for 3D simulations compared to 2D simulations. This is in contrast to Guo et al. (2014), who observed similar reconnection rates and energy conversion between 2D and 3D simulations, although the kink mode (Daughton 1999) strongly interacts with the tearing mode, leading to a turbulent reconnection layer (Yin et al. 2008). For particle acceleration in 3D reconnection simulations, early studies reported that the drift kink instability can modify the electric and magnetic field structures in an antiparallel reconnection layer and prohibit nonthermal acceleration (Zenitani & Hoshino 2005, 2007, 2008). However, recent large-scale 3D simulations have found that strong nonthermal particle spectra are produced even when the kink mode is active (Liu et al. 2011; Guo et al. 2014; Sironi & Spitkovsky 2014). Earlier large-scale 3D studies in nonrelativistic regimes also demonstrated the development of turbulence in the reconnection layer (Yin et al. 2008), but the influence on energetic particle acceleration is controversial, particularly in the relativistic regime.

In this paper, we perform 2D and 3D fully kinetic simulations starting from a force-free current sheet with uniform plasma density and temperature to model reconnection over a broad range in the magnetization parameter $\sigma = 0.25$ –1600. This paper builds upon earlier work (Guo et al. 2014) and gives further details regarding the plasma dynamics and particle acceleration during relativistic magnetic reconnection in the high- σ regime. We also present detailed results from a 3D simulation that shows a turbulent reconnection layer arising from the interaction between the secondary tearing and kink modes. In Section 2, we describe the numerical methods and parameters. Section 3 discusses the main results of the paper. In Section 4, we present an analytical model that explains the main feature of particle acceleration in the simulations. The implications from this work for a range of astrophysical problems are discussed in Section 5 and our conclusions are summarized in Section 6. In addition, we have also explicitly examined the numerical convergence for this

problem and the effect of numerical heating in our simulations, which is discussed in the [Appendix](#).

2. NUMERICAL METHODS

We envision a situation where intense current sheets are developed within a magnetically dominated plasma. Earlier work in nonrelativistic low- β plasmas has shown that the gradual evolution of the magnetic field can lead to formation of intense, nearly force-free current layers where magnetic reconnection may be triggered (Galsgaard et al. 2003; Titov et al. 2003). In the present study, the critical parameter is the magnetization parameter defined as $\sigma \equiv B^2/(4\pi n_e m_e c^2)$, which roughly corresponds to the available magnetic energy per particle. The numerical simulations presented in this paper are initialized from a force-free current layer with $\mathbf{B} = B_0 \tanh(z/\lambda)\hat{x} + B_0 \text{sech}(z/\lambda)\hat{y}$ (Che et al. 2011; Liu et al. 2013, 2014), which corresponds to a magnetic field with magnitude B_0 rotating by 180° across the central layer with a half-thickness of λ . No external guide field is included in this study but there is an intrinsic guide field B_y associated with the central sheet. The plasma consists of electron-positron pairs with mass ratio $m_i/m_e = 1$. The initial distributions are Maxwellian with a spatially uniform density n_0 and a thermal temperature ($kT_i = kT_e = 0.36m_e c^2$). Particles in the central sheet have a net drift $\mathbf{U}_i = -\mathbf{U}_e$ to represent a current density $\mathbf{J} = en_0(\mathbf{U}_i - \mathbf{U}_e)$ that is consistent with $\nabla \times \mathbf{B} = 4\pi\mathbf{J}/c$. Since the force-free current sheet does not require a hot plasma component to balance the Lorentz force, this initial setup is more suitable to study reconnection in low- β and/or high- σ plasmas. The full particle simulations are performed using the VPIC code (Bowers et al. 2009) and NPIC code (Daughton et al. 2006; Daughton & Karimabadi 2007), both of which solve Maxwell equations and push particles using relativistic approaches. The VPIC code directly evolves electric and magnetic fields, whereas in the NPIC code the fields are advanced using the scalar and vector potentials. Although the two codes have very different algorithms, all of the key results are in good agreement for this study, thus providing additional confidence in our conclusions. In addition, we have developed a particle-tracking module to analyze the detailed physics of the particle energization process. In the simulations, we define and adjust σ by changing the ratio of the electron gyrofrequency $\Omega_{ce} = eB/(m_e c)$ to the electron plasma frequency $\omega_{pe} = \sqrt{4\pi n e^2/m_e}$, $\sigma \equiv B^2/(4\pi n_e m_e c^2) = (\Omega_{ce}/\omega_{pe})^2$. For 2D simulations, we have performed simulations with $\sigma = 0.25 \rightarrow 1600$ and box sizes $L_x \times L_z = 300d_i \times 194d_i$, $600d_i \times 388d_i$, and $1200d_i \times 776d_i$, where d_i is the inertial length c/ω_{pe} . For 3D simulations, the largest case is $L_x \times L_y \times L_z = 300d_i \times 194d_i \times 300d_i$ with $\sigma = 100$. For high- σ cases ($\sigma > 25$), we choose cell sizes $\Delta x = \Delta y = 1.46/\sqrt{\sigma}d_i$ and $\Delta z = 0.95/\sqrt{\sigma}d_i$, so the particle gyromotion scale $\sim v_{the}/\sqrt{\sigma}d_i$ is resolved. The time step is chosen to correspond to a Courant number $C_r = c\Delta t/\Delta r = 0.7$, where $\Delta r = \Delta x\Delta y\Delta z/(\Delta x\Delta y + \Delta y\Delta z + \Delta x\Delta z)$. The half-thickness of the current sheet is $\lambda = 6d_i$ for $\sigma \leq 100$, $12d_i$ for $\sigma = 400$, and $24d_i$ for $\sigma = 1600$ in order to satisfy the drift velocity $U_i < c$. For both 2D and 3D simulations, we have more than 100 electron-positron pairs in each cell. The boundary conditions for 2D simulations are periodic for both fields and particles in the x direction, while in the z direction the boundaries are conducting for the field and reflecting for the particles. In the 3D

simulations, the boundary conditions are periodic for both fields and particles in the y direction, while the boundary conditions in the x and z directions are the same as in the 2D cases. A weak long-wavelength perturbation (Birn et al. 2001) with $B_z = 0.03B_0$ is included to initiate reconnection. The parameters for different runs are summarized in Table 1, which also lists key results such as maximum energy of particles, spectral index, the fraction of kinetic energy converted from the magnetic energy, and the portion of energy gain arising from the perpendicular electric fields.

Using the set of numerical parameters described above, all of the simulations show excellent energy conservation with violation of energy conservation less than 10^{-3} of the total energy in all cases. However, we note that to accurately determine the particle energy spectra, the violation in energy conservation should be smaller than the initial plasma kinetic energy, which is only a small fraction of the total energy for these problems. Caution is needed when using a small number of particles per cell and a small initial plasma kinetic energy in the simulations (Sironi & Spitkovsky 2014), since numerical heating may significantly modify the particle distribution. In the [Appendix](#), we have extensively tested how the numerical convergence varies with the initial plasma temperature, cell size, number of particles per cell, and time step. For all the cases we present in the main paper, the violation of energy conservation is a few per cent of the initial kinetic energy in the system, meaning that effects such as numerical heating have a negligible influence on the simulated energy spectra.

3. SIMULATION RESULTS

3.1. General Feature and Energy Conversion

Figure 1 gives an overview of the evolution of the current layer in the case with $\sigma = 100$ and domain size $L_x \times L_z = 300d_i \times 194d_i$ ($L_y = 300d_i$ for the 3D simulation) from runs 2D-7 and 3D-7. Panel (a) shows the color-coded current density from the 2D simulation and panel (b) shows a 2D cut of the current density and a 3D isosurface of plasma density colored by the current density from the 3D simulation at $\omega_{pe}t = 175$ and $\omega_{pe}t = 375$, respectively. Starting from the initial perturbation, the current sheet gradually narrows as the current density is concentrated in the central region. In the 2D simulation, the extended thin current sheet breaks into a number of fast moving secondary plasmoids ($\omega_{pe}t \sim 225$) due to the secondary tearing instability. The plasmoids coalesce and eventually merge into a single island at the edge of the simulation domain similar to the nonrelativistic case (Daughton & Karimabadi 2007). In the 3D simulation, as the intrinsic guide field associated with the force-free current layer is expelled from the central region, the kink instability (Daughton 1999) develops and interacts with the tearing mode, leading to a turbulent evolution (Yin et al. 2008). However, despite the strong 3D effects that modify the current layer, small-scale flux-rope-like structures with intense current density develop repeatedly as a result of the secondary tearing instability.

Although the plasma dynamics in the 2D and 3D simulations appears quite different, the energy conversion and particle energization are very similar. Figure 2(a) shows the evolution of magnetic energy E_B , electric field energy E_E , kinetic energy E_k , and energy carried by relativistic particles with $\gamma > 4$ from the 2D and 3D simulations (2D-7 and 3D-7). Note that, in both of these simulations, the total energy is conserved to within

Table 1
List of Simulation Runs with $\sigma \geq 6$

Run	σ	System Size	λ	p	γ_{\max}	$E_{\text{kin}}\%$	$(J \cdot E)_{\perp}\%$	$\alpha\tau_{\text{inj}}$
2D-1	6	$300d_i \times 194d_i$	$6d_i$	2.2	45	23%	83%	0.4
2D-2	6	$600d_i \times 388d_i$	$6d_i$	2.0	56	32%	92%	0.5
2D-3	6	$1200d_i \times 776d_i$	$6d_i$	1.7	79	34%	93%	0.7
2D-4	25	$300d_i \times 194d_i$	$6d_i$	1.6	195	28%	85%	1.1
2D-5	25	$600d_i \times 388d_i$	$6d_i$	1.3	339	37%	90%	1.6
2D-6	25	$1200d_i \times 776d_i$	$6d_i$	1.2	617	42%	90%	2.0
2D-7	100	$300d_i \times 194d_i$	$6d_i$	1.35	650	29%	73%	2.0
3D-7	100	$300d_i \times 194d_i \times 300d_i$	$6d_i$	1.35	617	28%	71%	N/A
2D-8	100	$600d_i \times 388d_i$	$6d_i$	1.25	1148	40%	78%	3.1
2D-9	100	$1200d_i \times 776d_i$	$6d_i$	1.15	1862	45%	94%	4.3
2D-10	400	$300d_i \times 194d_i$	$12d_i$	1.25	1514	20%	54%	3.0
2D-11	400	$600d_i \times 388d_i$	$12d_i$	1.15	3715	31%	75%	4.8
2D-12	400	$1200d_i \times 776d_i$	$12d_i$	1.1	5495	36%	86%	6.5
2D-13	1600	$300d_i \times 194d_i$	$24d_i$	1.2	2812	13%	45%	N/A
2D-14	1600	$600d_i \times 388d_i$	$24d_i$	1.1	7913	21%	53%	N/A
2D-15	1600	$1200d_i \times 776d_i$	$24d_i$	1.05	11220	30%	66%	N/A

Note. The spectral index p , the maximum energy (100-particle level) at the end of the simulation γ_{\max} , the percentage of magnetic energy that is converted into kinetic energy $E_{\text{kin}}\%$, the percentage of the conversion of magnetic energy caused by perpendicular electric field $(J \cdot E)_{\perp}\%$, and $\alpha\tau_{\text{inj}}$ estimated by tracking particles in the

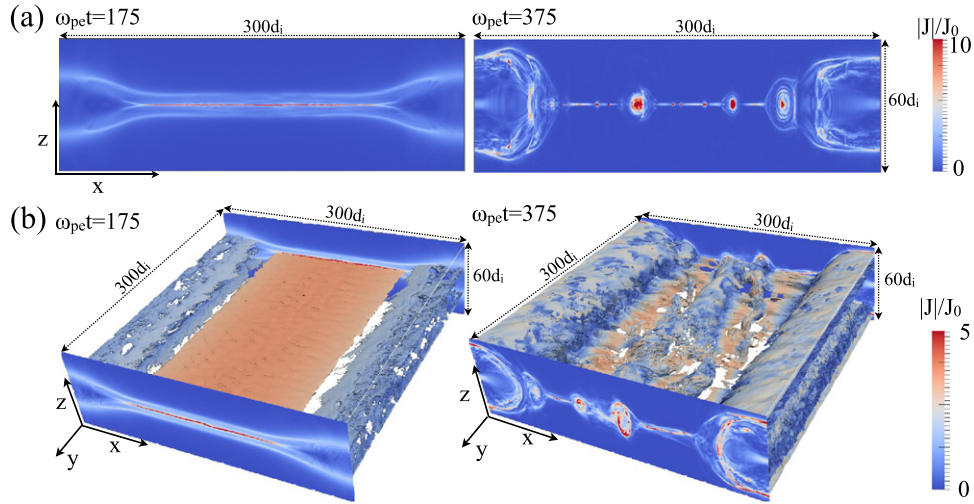


Figure 1. Evolution of 2D and 3D simulations with $\sigma = 100$ and domain size $L_x \times L_z = 300d_i \times 194d_i$ ($L_y = 300d_i$ for 3D): (a) color-coded current density from the 2D simulation at $\omega_{pe}t = 175$ and $\omega_{pe}t = 375$, respectively; (b) 2D cut of current density and a 3D isosurface of the plasma density colored by the current density at $\omega_{pe}t = 175$ and $\omega_{pe}t = 375$, respectively.

of the initial value. The evolutions of different forms of energies between 2D and 3D simulations are very similar. In both the 2D and 3D simulations, about 25% of the magnetic energy is converted into plasma kinetic energy, most of which is carried by relativistic particles. Figure 2(b) shows the time-integrated energy conversion from magnetic energy into plasma energy in the simulation $\int_0^t dt \int dV \mathbf{J} \cdot \mathbf{E}$ and its contribution from parallel and perpendicular electric field terms $\mathbf{J}_{\parallel} \cdot \mathbf{E}_{\parallel}$ and $\mathbf{J}_{\perp} \cdot \mathbf{E}_{\perp}$, respectively. Here $\int dV = \int dx dy dz$. The difference in energy conversion between the 2D and 3D simulations can be as large as a factor of 2 at $\omega_{pe}t = 300$, but at the end of the simulations both cases have converted about the same amount of magnetic energy. This shows that the kink instability that may modify the magnetic field does not significantly change the overall energy conversion. While the

energy conversion through parallel electric field is important when the thin current layer initially develops, most of the energy conversion is due to perpendicular electric fields induced by relativistic flows as the system is dominated by secondary plasmoids/flux ropes. This analysis has been done in all the cases and summarized in Table 1, which shows that the perpendicular electric field typically plays a dominant role in converting magnetic energy into plasma kinetic energy. This can also be seen in Figure 3, which shows the color-coded intensities of $\mathbf{J} \cdot \mathbf{E}$, $\mathbf{J}_{\perp} \cdot \mathbf{E}_{\perp}$, and $\mathbf{J}_{\parallel} \cdot \mathbf{E}_{\parallel}$ from the 2D and 3D simulations at $\omega_{pe}t = 175$ and $\omega_{pe}t = 375$, respectively. Figure 2(c) compares the energy spectra from the 2D and 3D simulations at various times. The most striking feature is that a hard power-law spectrum $f \propto (\gamma - 1)^{-p}$ with a spectral index $p \sim 1.35$ forms in both 2D and 3D runs. Although a fraction of particles are accelerated in the early phase when the parallel

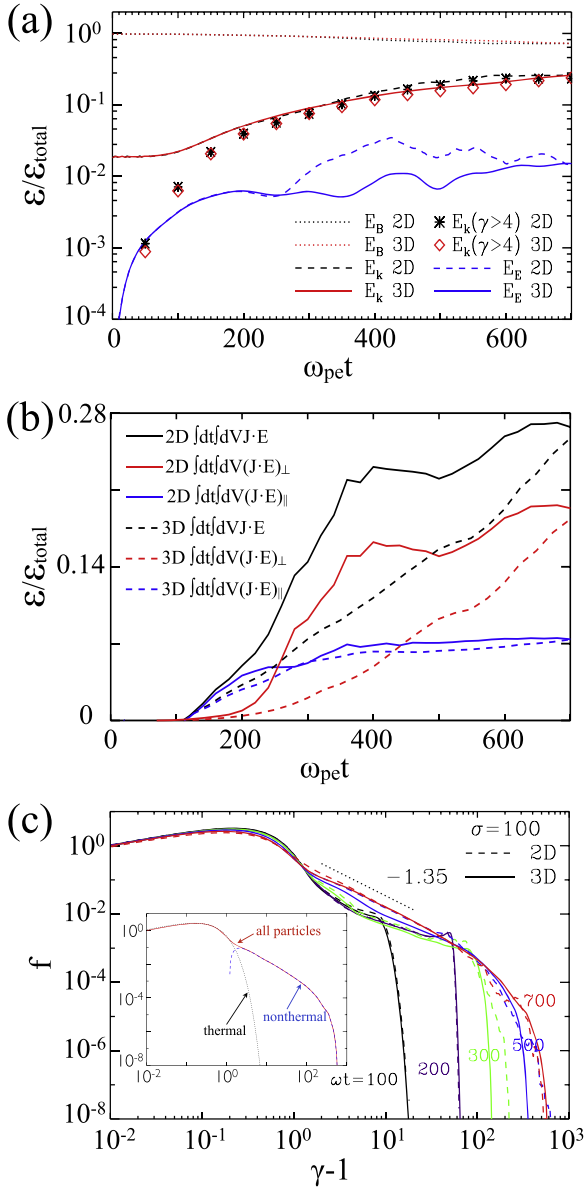


Figure 2. Plasma energetics in 2D and 3D simulations with $\sigma = 100$ and domain size $L_x \times L_z = 300d_i \times 194d_i$ ($L_y = 300d_i$ for 3D): (a) evolution of magnetic energy E_B , electric field energy E_E , plasma kinetic energy E_k , and energy carried by relativistic particles with Lorentz factor $\gamma > 4$; (b) energy conversion from magnetic energy into plasma energy integrated over time $\int_0^t dt dV \mathbf{J} \cdot \mathbf{E}$ and its contribution from parallel and perpendicular electric fields $\mathbf{J}_{\parallel} \cdot \mathbf{E}_{\parallel}$ and $\mathbf{J}_{\perp} \cdot \mathbf{E}_{\perp}$; (c) evolution of particle energy spectra from 2D and 3D simulations. Subpanel: energy spectrum from the 3D simulations at $\omega_{pe}t = 700$. The low energy is fitted with a thermal distribution and the rest of the distribution is a nonthermal power law with an exponential cut-off.

electric field is important, most of the particles in the power-law distribution are accelerated when the system is dominated by plasmoids/flux ropes. As we will discuss below, the formation of the power law is closely related to the motional electric field induced by the fast moving plasmoids. In the subpanel, the energy spectrum for all particles in the 3D simulation at $\omega_{pe}t = 700$ is shown by the red line. The low-energy portion can be fitted by a Maxwellian distribution (black) and the nonthermal part resembles a power-law distribution (blue) starting at $\gamma \sim 2$ with an exponential cut-off for $\gamma \gtrsim 100$. The nonthermal part contains $\sim 25\%$ of

particles and $\sim 95\%$ of the kinetic energy. The maximum particle energy of the system can be predicted approximately using the reconnecting electric field $m_e c^2 (\gamma_{\text{max}} - 1) = \int |qE_{\text{rec}}| c dt$ until the gyroradius is comparable to the system size (see also Figure 6(b)). Although we observe a strong kink instability in the 3D simulations, the energy conversion and particle energy spectra are remarkably similar to the 2D results, indicating that the 3D effects are not crucial for the particle acceleration. The fast acceleration is distinct from that of nonrelativistic magnetic reconnection, where particles are at most accelerated to mildly relativistic energy (e.g., Drake et al. 2006; Fu et al. 2006; Pritchett 2006; Oka et al. 2010). The nonthermal-dominated distribution in the simulations is also quite different from distributions in the relativistic shock regions (e.g., Spitkovsky 2008), where the particles are heated at the shock front and form an extended thermal distribution containing most of the dissipated energy. The power-law spectral index $p \sim 1$ from relativistic reconnection is significantly harder than the limit $p \sim 2$ predicted by nonrelativistic and relativistic shock acceleration theories (e.g., Blandford & Eichler 1987; Achterberg et al. 2001).

3.2. Particle Acceleration

We now discuss the details of particle acceleration. We will first present some analysis of particle trajectories to show the acceleration mechanism. Then the dominant acceleration mechanism is distinguished by tracking all the particles and calculating the energy gain using the guiding-center drift approximation. The results demonstrate that the dominant acceleration mechanism is a first-order Fermi acceleration through curvature drift motion along the motional electric field induced by the relativistic reconnection flows. We calculate the acceleration rate $\alpha = \Delta\epsilon/(\epsilon\Delta t)$ and its time integral for cases with $\sigma = 6-400$, where $\Delta\epsilon$ is the averaged energy gain for particles of energy ϵ over a period Δt . Finally, we summarize the character of the energy spectra. These main results will be discussed and interpreted in detail in Section 4, where we present the acceleration model.

Figures 4 and 5 present the trajectory analysis for the motions of accelerated particles in the 2D case with $\sigma = 100$ and $L_x \times L_z = 600d_i \times 388d_i$. These particles were selected to show the characteristic trajectories of accelerated particles, which are consistent with the results of the statistical analysis in Figure 6. The first three panels of Figure 4 show (a) the trajectory of a representative particle close to the central sheet between $\omega_{pe}t = 30-300$ together with E_{\parallel} at $\omega_{pe}t = 180$, (b) the trajectory of the same particle between $\omega_{pe}t = 310-510$ together with E_y at $\omega_{pe}t = 400$, and (c) the trajectory of the particle between $\omega_{pe}t = 510-720$ together with E_y at $\omega_{pe}t = 640$. The starting and ending locations of the particle are labeled by “+” and “x” signs, respectively. Note that the field is highly variable in time and the location of the particle at the same time step as the field contour is drawn by the “*” sign. The two bottom panels show the evolution of the particle energy as a function of time (d) and energy as a function of the x position (e). Each period corresponding to that in (a)–(c) is labeled by the same color. The green curve represents the energy gain in the parallel electric field integrated from $t = 0$. Initially the particle is close to the central layer and gains energy by the parallel electric field. It is then strongly accelerated by the perpendicular electric field when the

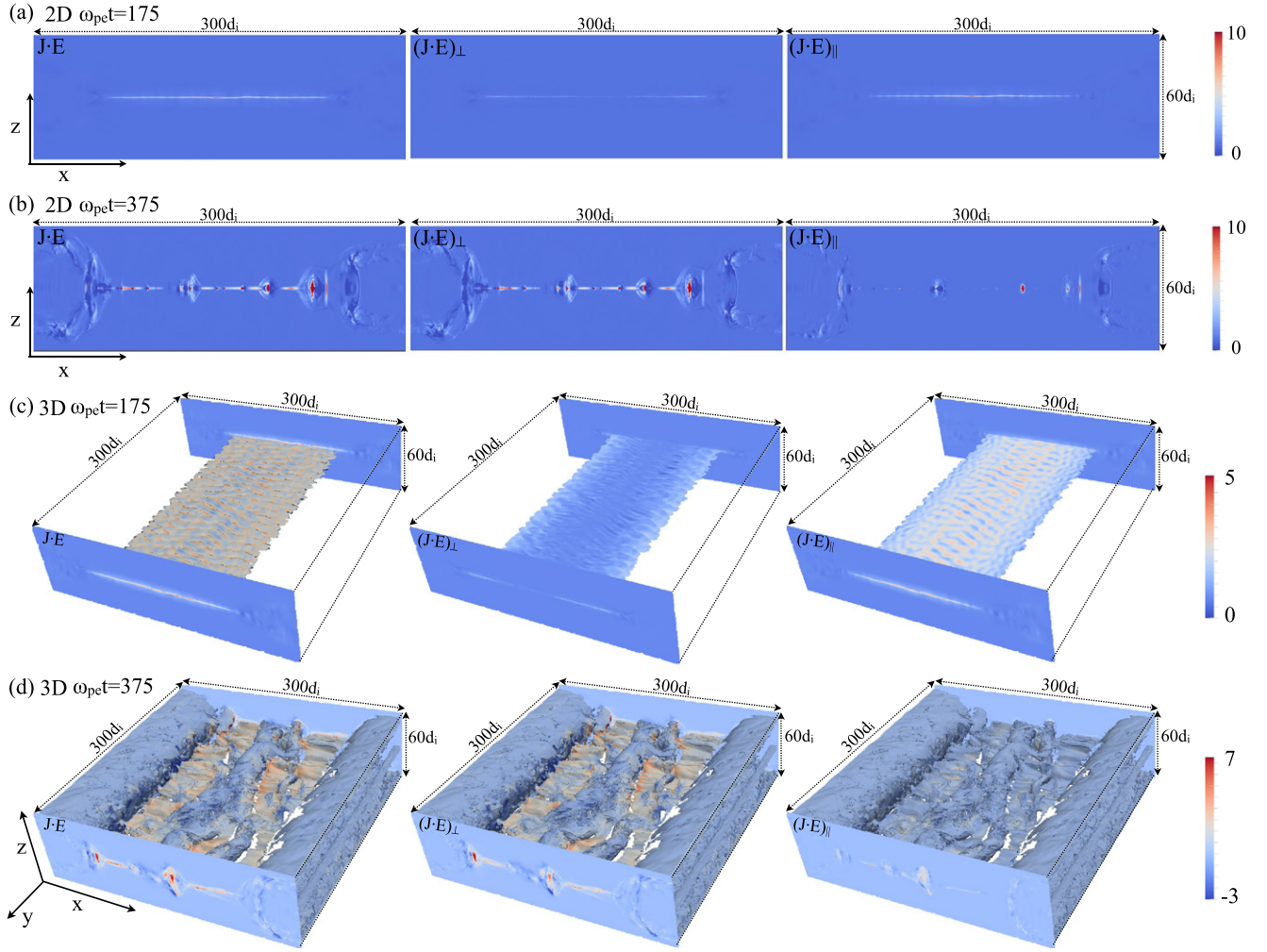


Figure 3. Color-coded intensity of energy conversion rate $\mathbf{J} \cdot \mathbf{E}$ normalized using $n_0 m_e c^2 \omega_{pe}$ and contributions from $\mathbf{J}_\perp \cdot \mathbf{E}_\perp$ and $\mathbf{J}_\parallel \cdot \mathbf{E}_\parallel$ for the 2D and 3D simulations with $\sigma = 100$ at $\omega_{pe} t = 175$ and $\omega_{pe} t = 375$, respectively. In the early stage the conversion by parallel electric field is important and the perpendicular electric field plays a dominant role when multiple plasmoids (flux ropes in 3D) develop due to the secondary tearing instability.

reconnection region breaks into multiple islands. This electric field is predominantly due to the motional effect $\mathbf{E} = -\mathbf{V} \times \mathbf{B}/c$ generated by relativistic plasma outflows. The figure also shows that the acceleration by \mathbf{E}_\perp resembles a Fermi process as particles bounce back and forth within a magnetic island.

Figure 5 presents another view of the particle acceleration physics. It is similar to Figure 4, but the field contours show the outflow speed to highlight the role of V_x in the particle's energization. This clearly illustrates a relativistic first-order Fermi process by bouncing in outflow regions of the reconnection layer. Note that the energy gain from the parallel electric field for this sample particle is negligible since it entered the reconnection layer after the development of multiple plasmoids.

In Figure 6, we present more analysis to illustrate the mechanism of the particle acceleration. Panel (a) shows the energy as a function of the x position of four accelerated particles. Similar to Figure 5, the electrons gain energy by bouncing back and forth within the reconnection layer. In addition, we have analyzed trajectories of a large number of particles and found the energy gain for each cycle is $\Delta\epsilon \sim \epsilon$, which demonstrates that the acceleration mechanism is a first-

order Fermi process (Drake et al. 2006, 2010; Kowal et al. 2011). Panel (b) shows the maximum particle energy in the system as a function of time. This is plotted using different count levels from the 1-particle level to the 1000-particle level. Also plotted is the estimated maximum energy resulting from the reconnecting electric field by assuming particles moving along the electric field at the speed of light $\int |qE_{\text{rec}}| c dt$. This shows that the maximum possible energy occurs for a small number of particles that continuously sample the reconnection electric field $m_e c^2 \gamma_{\text{max}} = \int |qE_{\text{rec}}| c dt$. At late time, as the particle gyroradius becomes large and comparable to the system size, the maximum energy saturates. To show the Fermi process more rigorously, we have tracked the energy change for all the particles in the simulation and the relative contributions arising from the parallel electric field ($m_e c^2 \Delta\gamma = \int q v_\parallel E_\parallel dt$) and curvature drift acceleration ($m_e c^2 \Delta\gamma = \int q \mathbf{v}_{\text{curv}} \cdot \mathbf{E}_\perp dt$) similar to Dahlin et al. (2014), where $\mathbf{v}_{\text{curv}} = \gamma v_\parallel^2 (\mathbf{b} \times (\mathbf{b} \cdot \nabla) \mathbf{b}) / \Omega_{ce}$, v_\parallel is the particle velocity parallel to the magnetic field, and $\mathbf{b} = \mathbf{B}/|B|$. Panel (c) shows the averaged energy gain and the contribution from parallel electric field and curvature drift

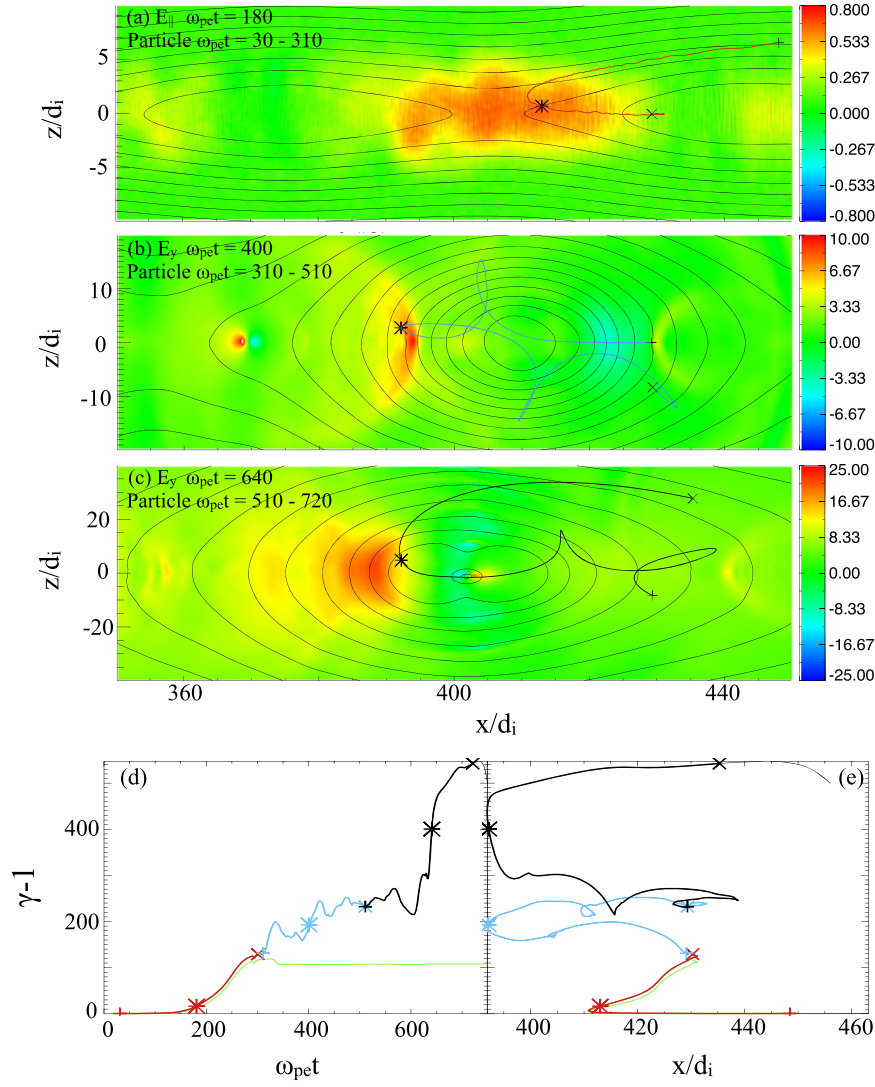


Figure 4. Panels (a)–(c) show a particle trajectory in the x – z plane together with the color-coded electric field (a) E_{\parallel} , (b) E_y , and (c) E_x . Panels (d) and (e) show the particle energy as a function of time and energy as a function of the x position, respectively. In (d) and (e), curves with different colors represent the energy evolution during time periods in (a)–(c). The green curve shows the integrated energy gain from the parallel electric field.

acceleration over an interval of $25\omega_{pe}^{-1}$ as a function of energy starting at $\omega_{pe}t = 350$. The energy gain follows $\Delta\epsilon \sim \alpha\epsilon$, confirming the first-order Fermi process identified from particle trajectories. The energy gain from the parallel motion depends weakly on energy, whereas the energy gain from the curvature drift acceleration is roughly proportional to energy. In the early phase, the parallel electric field is strong but only accelerates a small portion of particles, and the curvature drift dominates the acceleration starting at about $\omega_{pe}t = 250$. The contribution from the gradient drift was also evaluated and found to be negligible in comparison. Panel (d) shows $\alpha = \langle \Delta\epsilon \rangle / (\epsilon \Delta t)$ measured directly from the energy gain of the particles in the perpendicular electric field ($m_e c^2 \Delta\gamma = \int q \mathbf{v}_{\perp} \cdot \mathbf{E}_{\perp} dt$) and estimated from the expression for the curvature drift acceleration. The close agreement demonstrates that the curvature drift term dominates the particle energization.

For higher σ and larger domains, the acceleration is stronger and reconnection is sustained over a longer duration. In Figure 7(a), we present the final energy spectra for a number of cases with different σ and system size $L_x \times L_z = 600d_i \times 388d_i$. A

summary for the spectral index can also be found in Table 1. In Figure 7(b), a summary for the measured spectral index for the power-law ranges of all the 2D runs shows that the spectrum is harder for higher σ and larger domain sizes, and approaches the limit $p = 1$. Note that the spectral indices appear systematically harder than in other recent papers (Melzani et al. 2014b; Sironi & Spitkovsky 2014; Werner et al. 2014). However, the energy spectra in these studies are plotted using total relativistic energy γmc^2 and here we use kinetic energy $(\gamma - 1)mc^2$. Using total relativistic energy in the energy spectra significantly distorts the spectral index in the energy range $0 < \gamma - 1 < 10$, which may alter the interpretation of the results (Melzani et al. 2014b; Sironi & Spitkovsky 2014; Werner et al. 2014).³

³ In fact, our simulation results show that the “–1” spectra can be obtained as long as the magnetic energy dominates over the initial plasma kinetic energy $8\pi nkT_0/B^2 = \beta \ll 1$. An example can be seen in the appendix (Figure 13), which robustly shows that the $p = 1$ spectrum can be obtained when $\sigma = 25$ and $kT_0 = 0.01mc^2$. The same spectrum gives a “ $p \sim 2$ ” slope when it is plotted as a function of γ , which may explain the different conclusions reported by other papers (Melzani et al. 2014b; Sironi & Spitkovsky 2014; Werner et al. 2014).

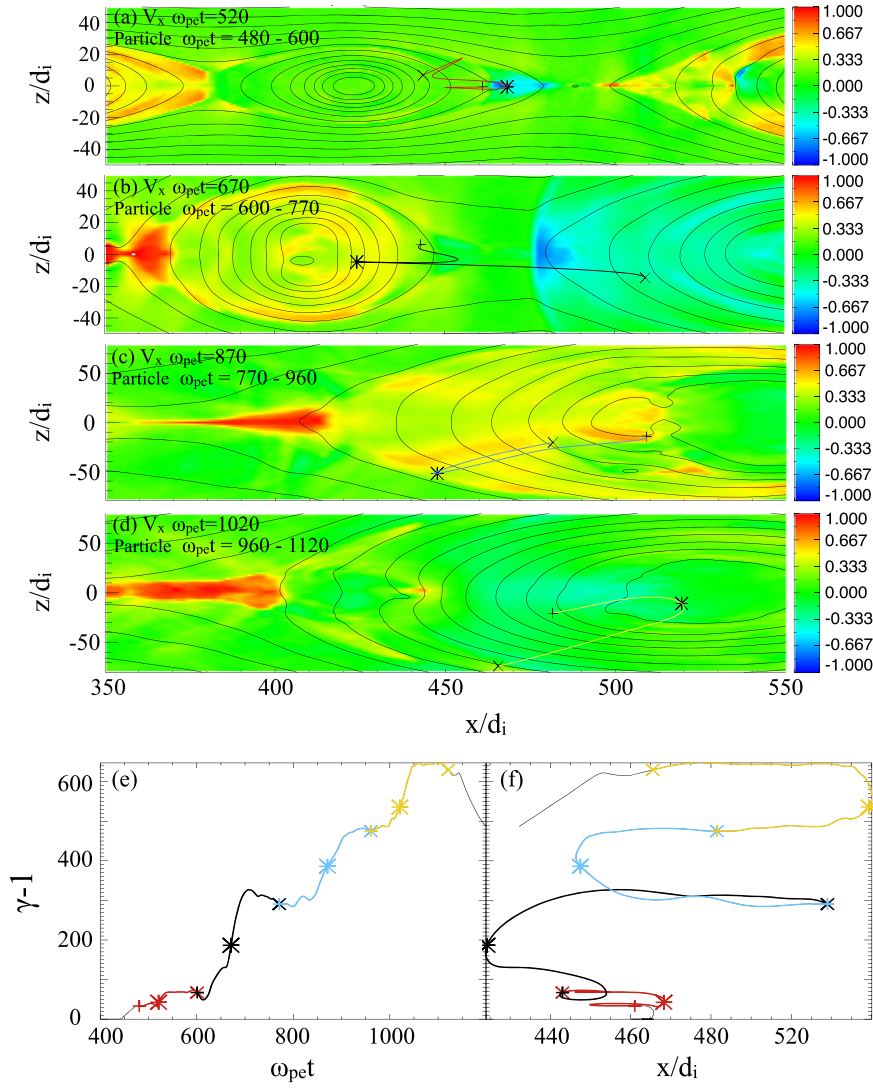


Figure 5. Panels (a)–(d) show a particle trajectory in the x – z plane together with the fluid velocity in the x direction V_x . Panels (e) and (f) show the particle energy as a function of time and energy as a function of the x position, respectively. Different colored curves represent the energy evolution during time periods in (a)–(d), showing that the particle gains energy by bouncing in the relativistic flow generated by reconnection.

3.3. Reconnection Rate and Relativistic Flows

Figure 8(a) shows the time-dependent reconnection rates normalized using the initial asymptotic magnetic field B_0 in 2D and 3D simulations with $\sigma = 100$ (runs 2D-7 and 3D-7). The 2D reconnection rate is computed from

$$R = \frac{E_{\text{rec}}}{B_0} = \frac{1}{B_0 V_{A0}} \left\langle \frac{\partial \psi}{\partial t} \right\rangle,$$

where $\psi = \max(A_y) - \min(A_y)$ along the central layer $z = 0$, A_y is the vector potential along the y direction, $\langle \rangle$ represents a time average over $\delta t \omega_{\text{pe}} = 25$ (Liu et al. 2014), and $V_{A0} = v_A / \sqrt{1 + (v_A/c)^2} = \sqrt{\sigma/(2 + \sigma)} c$ is the relativistic Alfvén speed in the cold-plasma limit. Here $v_A = B_0 / \sqrt{4\pi n(m_i + m_e)}$ is the nonrelativistic Alfvén speed based on B_0 . The 3D reconnection rate is estimated by using the mixing of plasma across the separatrix surfaces (Daughton et al. 2014). The rate in the 2D simulation is quite variable but the range is within a factor of 2 of the 3D rate. Figure 8(b) shows the

peak reconnection rate for a number of 2D cases with σ from 0.25 to 1600 and box size $1200d_i \times 776d_i$. The rate is observed to increase with σ from $E_{\text{rec}} \sim 0.03B_0$ for $\sigma = 1$ to $E_{\text{rec}} \sim 0.24B_0$ for $\sigma = 1600$. These results show that the peak reconnection field increases with σ and starts to saturate around $\sigma = 1000$. For low- σ cases with $\sigma < 1$, the reconnecting electric field is consistent with previous work for nonrelativistic reconnection (e.g., Daughton & Karimabadi 2007). More detailed analyses have shown that for high- σ cases, the reconnection rate normalized using the magnetic field B_u upstream of the diffusion region E_{rec}/B_u is close to 1 for $\sigma \gtrsim 100$ (Liu et al. 2015).

In Figures 9(a) and (b) we plot the maximum flow velocity in the x direction (outflow direction) and the corresponding Lorentz factor Γ_x . The 2D results are represented by blue symbols and the 3D results are in red symbols. Although we have only used a small simulation domain that may be affected by counter-streaming particles, a relativistic outflow still develops with Γ_x of a few. In Figures 9(c) and (d) we plot the maximum flow velocity in the z direction (inflow direction) and the corresponding Lorentz factor Γ_z , respectively.

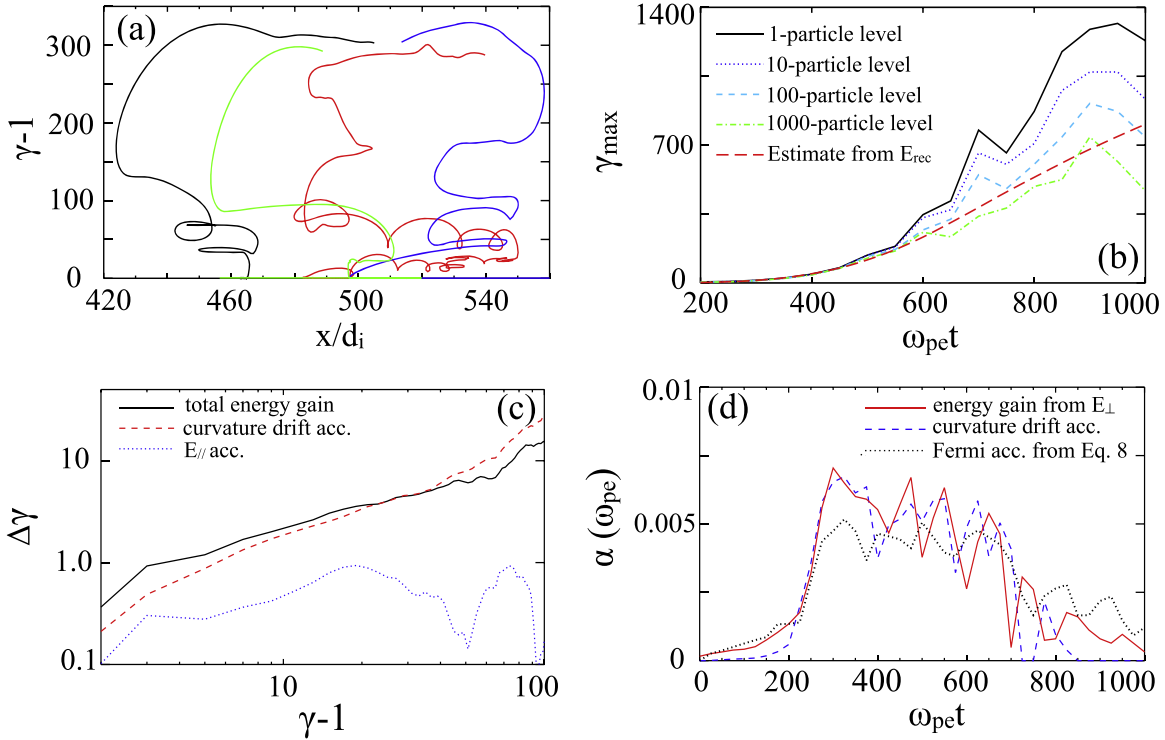


Figure 6. (a) Energy as a function of x position of four accelerated particles; (b) the maximum energy of particles in the system as a function of time from the 1-particle count level to the 1000-particle level. The red dashed line shows the maximum energy estimated for a particle moving in the direction of the reconnecting electric field at the speed of light $m_e c^2 \gamma_{\max} = \int |q E_{rec}| c dt$; (c) averaged energy gain and contributions from parallel electric fields and curvature drift acceleration over a time interval of $25 \omega_{pe}^{-1}$ as a function of particle energy starting at $\omega_{pe} t = 350$; (d) $\alpha = \langle \Delta \epsilon \rangle / (\langle \epsilon \rangle \Delta t)$ from energy gain in the perpendicular electric field and by curvature drift acceleration, and from Equation (6) using the averaged flow speed and island size.

Interestingly, the inflow speed can also be relativistic for high- σ cases. Detailed analysis for the diffusion region has been discussed in Liu et al. (2015), which shows that the inflow speed can be predicted by a model based on the Lorentz contraction of the plasma passing through the diffusion region.

The enhanced reconnection rate and development of relativistic inflow/outflow structures are in contrast to earlier results (Sironi & Spitkovsky 2014), where the observed outflows were only mildly relativistic and the inflow remained nonrelativistic. Note that Liu et al. (2015) have also reported the development of relativistic inflow for both Harris and force-free current sheets, indicating that this property of relativistic magnetic reconnection does not strongly depend on the initial setup.

3.4. 3D Dynamics

In our 3D simulation, we also find that relativistic outflows with $\Gamma_x \sim 4$ can develop in the system. Figure 10 shows the power spectrum of magnetic fluctuations with wave numbers perpendicular to the y direction and a volume rendering of the current density in the 3D simulation with $\sigma = 100$ at $\omega_{pe} t = 708$. The power spectrum shows a clear inertial range with a slope of “-2” and steeper slope for higher wave numbers $k_{\perp} d_i \gtrsim 1$. As we have discussed, the 3D simulation allows the development and interaction of secondary tearing instability and kink instability, leading to a turbulent magnetic field in the reconnection layer. Throughout these simulations, the range of scales for the 2D magnetic islands is similar to the observed 3D flux ropes. The maximum energy in both 2D and 3D agrees well with the time integral of energy gain from the reconnecting electric field. The energy distributions

reported in this paper are remarkably similar in 2D and 3D, suggesting that the underlying Fermi acceleration is rather robust and does not depend on the existence of well-defined magnetic islands.

4. A SIMPLE MODEL

It is often argued that some loss mechanism is needed to form a power-law distribution (Zenitani & Hoshino 2001; Drake et al. 2010, 2013; Hoshino 2012). However, the simulation results reported in this paper clearly show power-law distributions in a closed periodic system. Here we present a simple model to explain the power-law energy spectrum observed in our particle-in-cell (PIC) simulations. The model is illustrated by Figure 11(a). As reconnection proceeds, cold plasma in the upstream region advects into the acceleration zone at a constant velocity that is determined by reconnection electric field $V_{in} = c E_{rec} \times \mathbf{B} / B^2$. The process lasts $\tau \sim L_z / 2 V_{in}$, where L_z is the size of the simulation box along the z direction. In the acceleration region, our analysis has shown that a first-order Fermi process dominates the energy gain during reconnection. We solve the energy-continuity equation for the energy distribution function $f(\epsilon, t)$ within the acceleration region

$$\frac{\partial f}{\partial t} + \frac{\partial}{\partial \epsilon} \left(\frac{\partial \epsilon}{\partial t} f \right) = 0, \quad (1)$$

with acceleration $\partial \epsilon / \partial t = \alpha \epsilon$, where $\epsilon = m_e c^2 (\gamma - 1) / kT$ is the normalized kinetic energy and α is the constant acceleration rate in the first-order Fermi process. We assume that the initial distribution within the layer f_0 is Maxwellian with initial

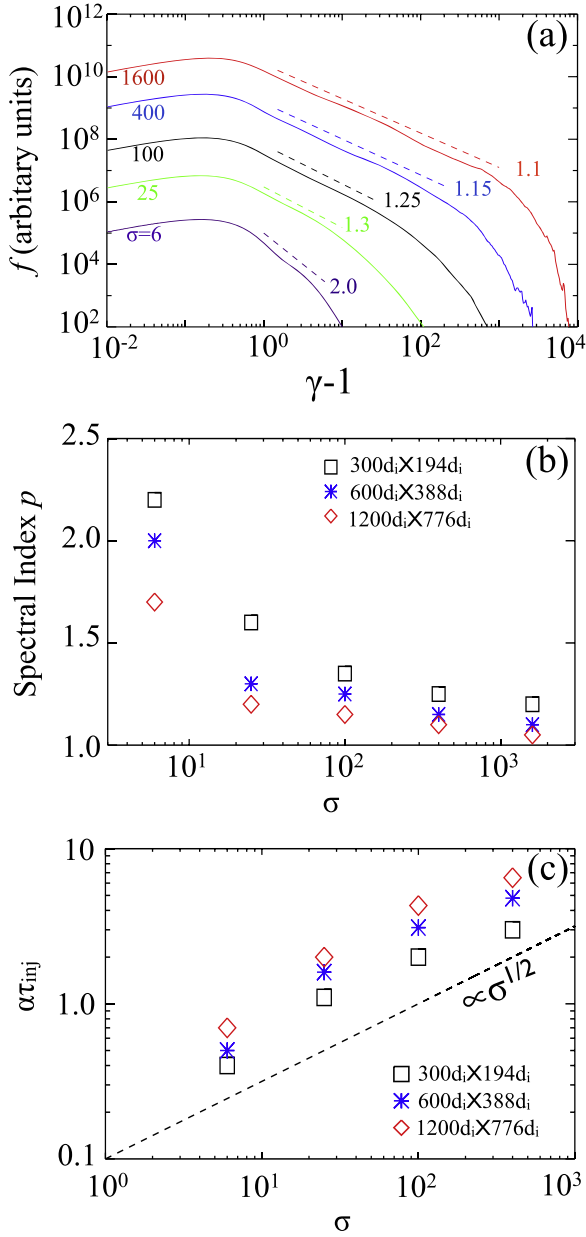


Figure 7. Energy spectra at the end of simulations for a series of 2D runs with system size $L_x \times L_z = 600d_i \times 388d_i$ and different σ from 6 to 1600. (b) Spectral index for all 2D simulations with σ from 6 to 1600. (c) Time-integrated $\alpha\tau_{inj}$ for cases with $\sigma = 6$ –400 and different system sizes.

temperature $kT < m_e c^2$, such that

$$f_0 \propto \gamma(\gamma^2 - 1)^{1/2} \exp(-\varepsilon) \approx \sqrt{2\varepsilon} \left(1 + \frac{5kT}{4m_e c^2} \varepsilon + \dots \right) \exp(-\varepsilon). \quad (2)$$

For simplicity, we consider the lowest order (nonrelativistic) term in this expansion and normalize $f_0 = \frac{2N_0}{\sqrt{\pi}} \sqrt{\varepsilon} \exp(-\varepsilon)$ by the number of particles N_0 within the initial layer. The distribution after time t is

$$f(\varepsilon, t) = \frac{2N_0}{\sqrt{\pi}} \sqrt{\varepsilon} e^{-3\alpha t/2} \exp(-\varepsilon e^{-\alpha t}), \quad (3)$$

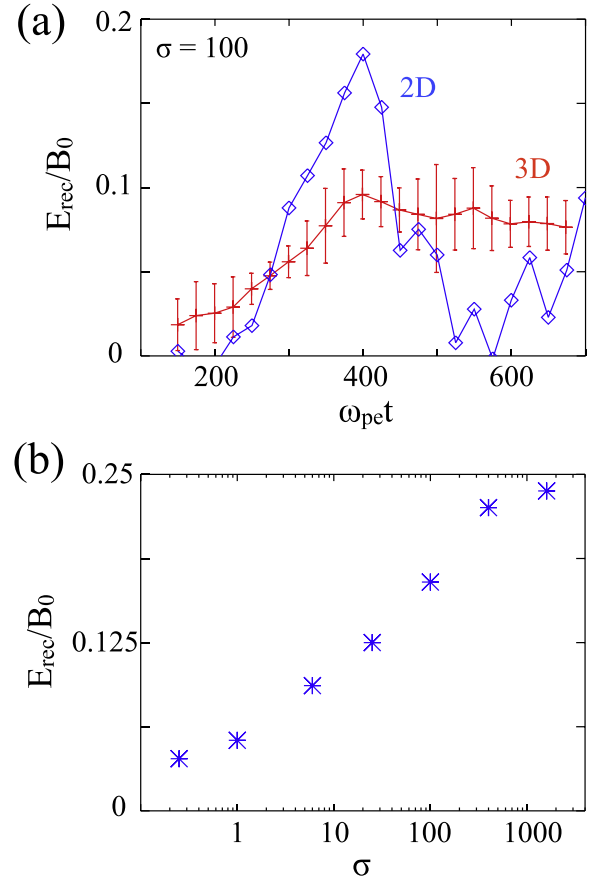


Figure 8. (a) Time-dependent 2D and 3D reconnection electric field normalized by the initial magnetic field E_{rec}/B_0 . (b) Normalized peak electric field E_{rec}/B_0 as a function of σ in 2D simulations.

which remains a thermal distribution with a temperature $e^{\alpha t} T$, consistent with that obtained by Drake et al. (2010). However, since upstream particles enter continuously into the acceleration region, the number of particles in the acceleration zone increases with time. We consider a particle distribution

$f_{inj} = \frac{2N_{inj}}{\sqrt{\pi}} \sqrt{\varepsilon} \exp(-\varepsilon)$ with number of particles $N_{inj} \propto V_{in} \tau_{inj}$ injected from upstream, where τ_{inj} is the timescale for particle injection. To highlight the key role that time-dependent injection plays in setting up the power law, we first consider a quick heuristic derivation of the main result. To proceed, we split f_{inj} into N groups and release the j th group into the acceleration region at time $t = j\Delta t$. Since each group will satisfy Equation (3) for a different initial time, after we have injected the final group at $t = \tau_{inj}$, the total distribution (in the limit $N \rightarrow \infty$) is

$$f(\varepsilon, t) \sim \frac{2N_{inj}}{\sqrt{\pi} \tau_{inj}} \int_0^{\tau_{inj}} \sqrt{\varepsilon} e^{-3\alpha t/2} \exp(-\varepsilon e^{-\alpha t}) dt = \frac{N_{inj}}{\alpha \tau_{inj}} \left[\frac{\text{erf}(\varepsilon^{1/2}) - \text{erf}(\varepsilon^{1/2} e^{-\alpha \tau_{inj}/2})}{\varepsilon} + \frac{2}{\sqrt{\pi}} \frac{e^{-\alpha \tau_{inj}/2} \exp(-\varepsilon e^{-\alpha \tau_{inj}}) - e^{-\varepsilon}}{\varepsilon^{1/2}} \right]. \quad (4)$$

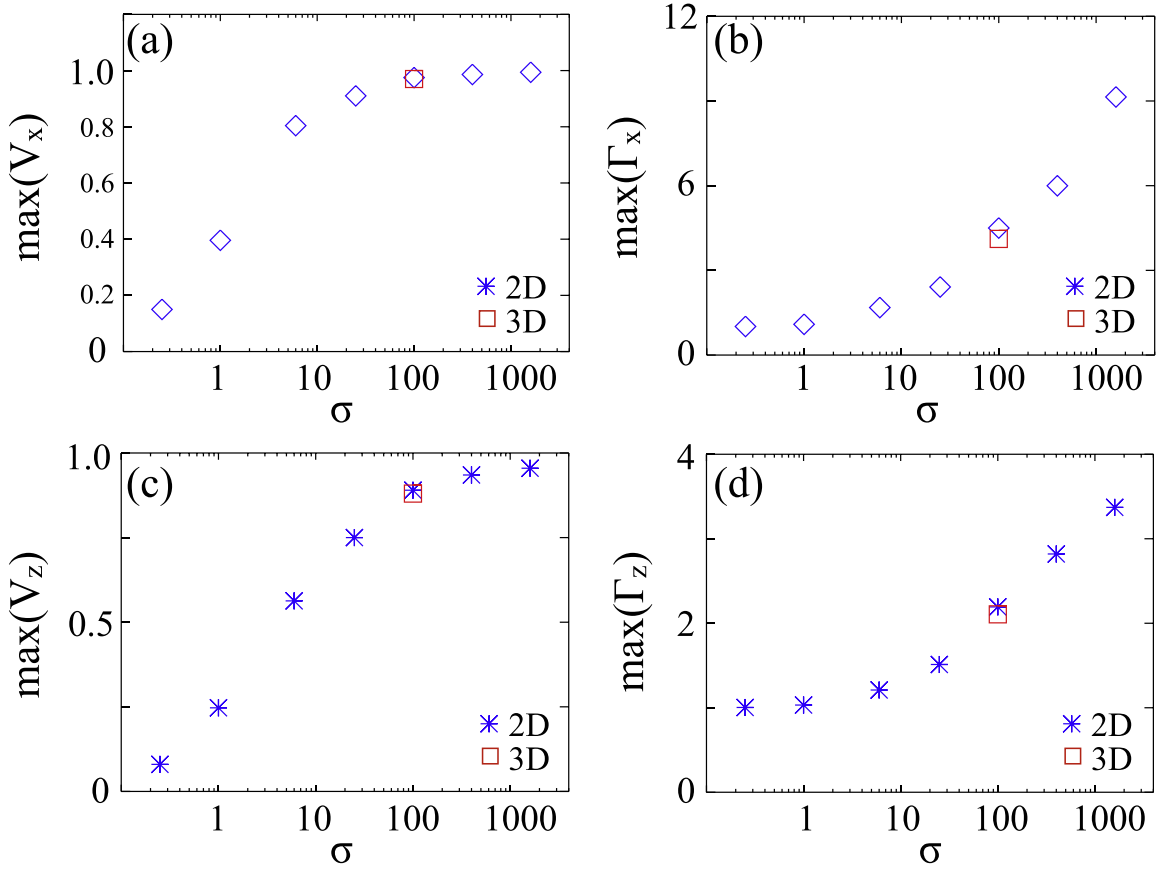


Figure 9. (a) Maximum flow velocity in the x direction V_x as a function of σ ; (b) the maximum flow Lorentz factor in the x direction $\Gamma_x = 1/(1 - V_x^2/c^2)$ as a function of σ ; (c) the maximum flow velocity in the z direction V_z as a function of σ ; (d) the maximum flow Lorentz factor in the z direction $\Gamma_z = 1/(1 - V_z^2/c^2)$ as a function of σ .

In the limit of $\alpha\tau \gg 1$, this gives the relation $f \propto 1/\varepsilon$ in the energy range $1 < \varepsilon < e^{\alpha\tau_{\text{inj}}}$. Figure 11(b) shows (4) for different $\alpha\tau_{\text{inj}}$. A power-law spectrum with $p = 1$ emerges as $\alpha\tau_{\text{inj}}$ increases $\alpha\tau_{\text{inj}} > 1$. Note that for a closed system, since the averaged magnetic energy per particle is only $\sigma m_e c^2/4$ and the energy in each energy bin is constant, the maximum energy of the power law can only extend to $\gamma_{\text{max}} \sim \sigma/4$.

Next, in order to treat the problem more rigorously, and include the influence of particle escape, we consider the more complete equation

$$\frac{\partial f}{\partial t} + \frac{\partial}{\partial \varepsilon} \left(\frac{\partial \varepsilon}{\partial t} f \right) = \frac{f_{\text{inj}}}{\tau_{\text{inj}}} - \frac{f}{\tau_{\text{esc}}}, \quad (5)$$

where τ_{esc} is the escape time for particles. For the initial current-layer distribution f_0 and injected particle distribution f_{inj} considered above, the solution can be written as

$$\begin{aligned} f(\varepsilon, t) = & \frac{2N_0}{\sqrt{\pi}} \sqrt{\varepsilon} e^{-(3/2+\beta)\alpha t} \exp(-\varepsilon e^{-\alpha t}) \\ & + \frac{2N_{\text{inj}}}{\sqrt{\pi} (\alpha\tau_{\text{inj}}) \varepsilon^{1+\beta}} \left[\Gamma_{(3/2+\beta)}(\varepsilon e^{-\alpha t}) \right. \\ & \left. - \Gamma_{(3/2+\beta)}(\varepsilon) \right], \end{aligned} \quad (6)$$

where $\beta = 1/(\alpha\tau_{\text{esc}})$ and $\Gamma_s(x)$ is the incomplete Gamma function. The first term accounts for particles initially in the acceleration region while the second term describes the evolution of injected particles. In the limit of no injection or escape ($\tau_{\text{esc}} \rightarrow \infty$ and $\tau_{\text{inj}} \rightarrow \infty$), the first term in (6) remains a thermal distribution the same as (3). However, as reconnection proceeds new particles enter continuously into the acceleration region and due to the periodic boundary conditions there is no particle escape. Thus considering the case $\tau_{\text{esc}} \rightarrow \infty$ and assuming $N_0 \ll N_{\text{inj}}$, at the time $t = \tau_{\text{inj}}$ when reconnection saturates the second term in (6) simplifies to (4). Thus in the limit $N_0 \sim N_{\text{inj}}$ the first term in (6) should be retained and the power-law produced is sub-thermal relative to this population. While it is straightforward to obtain the relativistic corrections arising from the injected distribution (2), we emphasize that these terms do not alter the spectral index. This solution explains results from our simulations, and also appears to explain the results from several recent papers, which obtained power-law distributions by subtracting the initial hot plasma component in the current layer (Melzani et al. 2014b; Sironi & Spitkovsky 2014; Werner et al. 2014). In particular, Melzani et al. (2014b) explicitly discussed the evolution of particle distribution initially in the current layer and reported it as a heated Maxwellian distribution.

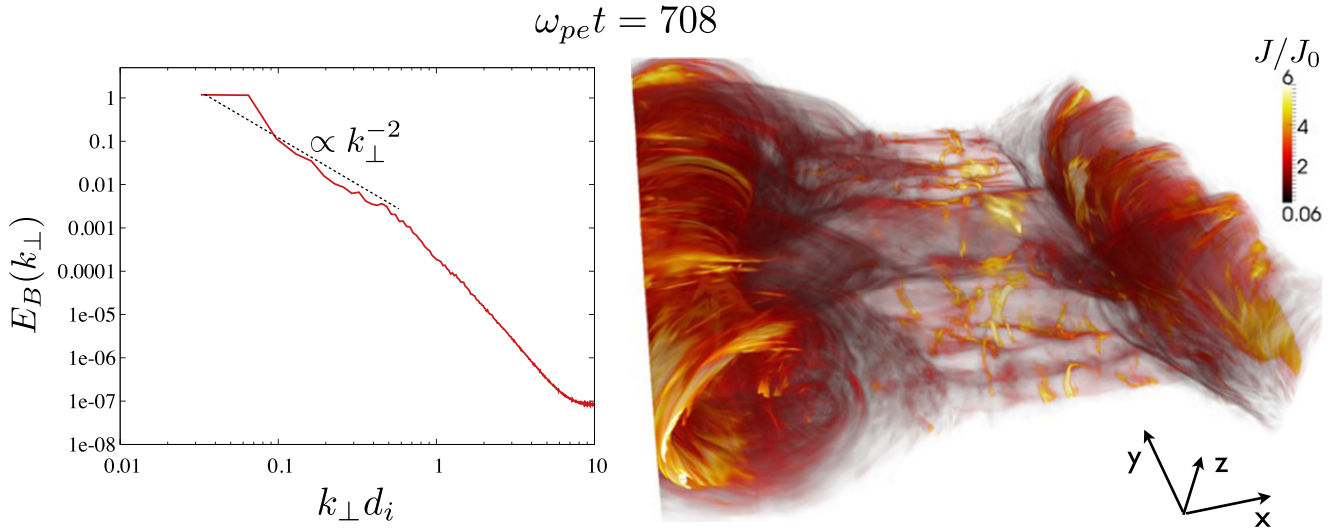


Figure 10. Evidence for turbulence in the 3D simulation. Left: power spectrum of magnetic fluctuations with wave numbers perpendicular to the y direction. Right: volume rendering of the current density J/J_0 in the 3D simulation at $\omega_{pe}t = 708$.

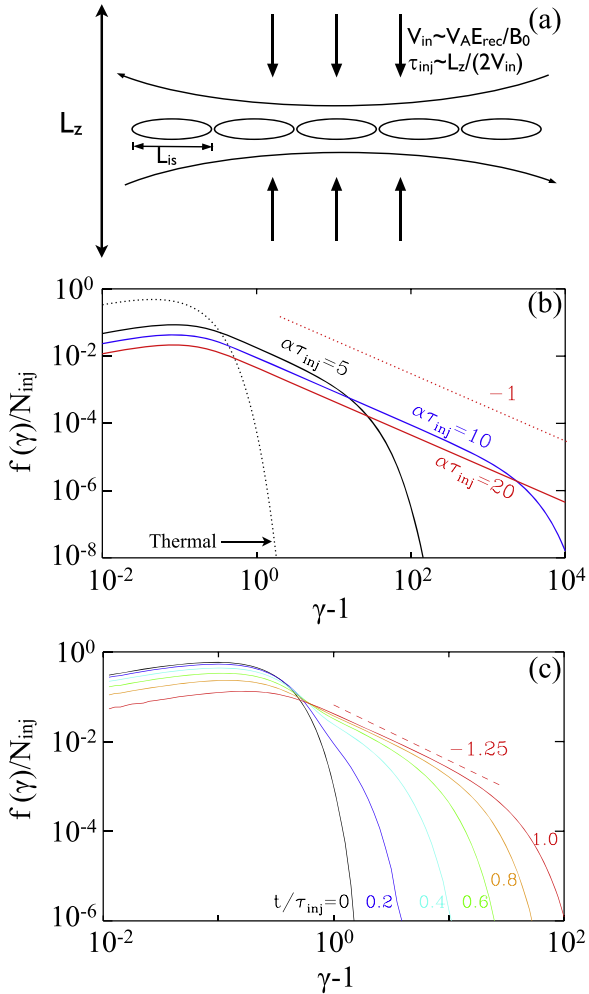


Figure 11. (a) Illustration of the acceleration model for the formation of power-law distributions. (b) Analytical results for different $\alpha\tau_{inj}$ obtained from Equation (4). (c) The solution of Equation (1) using time-dependent $\alpha(t)$ from Figure 6(d).

In order to estimate the acceleration rate α , the energy change of each particle can be approximated by a relativistic collision formula (e.g., Longair 1994)

$$\Delta\varepsilon = \left[\Gamma_V^2 \left(1 + \frac{2Vv_x}{c^2} + \frac{V^2}{c^2} \right) - 1 \right] \varepsilon, \quad (7)$$

where V is the outflow speed, $\Gamma_V^2 = 1/(1 - V^2/c^2)$, and v_x is the particle velocity in the x direction. The time between two collisions is about L_{is}/v_x , where L_{is} is the typical size of the magnetic islands (or flux ropes in 3D). Assuming that relativistic particles have a nearly isotropic distribution $v_x \sim c/2$, then

$$\alpha = \frac{\Delta\varepsilon}{\varepsilon\Delta t} \sim \frac{c \left(\Gamma_V^2 \left(1 + \frac{V}{c} + \frac{V^2}{c^2} \right) - 1 \right)}{2L_{is}}. \quad (8)$$

Using this expression, we measure the averaged V and L_{is} from the simulations and estimate the time-dependent acceleration rate $\alpha(t)$. An example is shown in Figure 6(d). This agrees reasonably well with that obtained from perpendicular acceleration and curvature drift acceleration. Figure 7(c) shows the time-integrated value of $\alpha\tau_{inj} = \int_0^{\tau_{inj}} \alpha(t)dt$ for various simulations with $\sigma = 6-400$. For cases with $\alpha\tau_{inj} > 1$, a hard power-law distribution with spectral index $p \sim 1$ forms. For higher σ and larger system size, the magnitude of $\alpha\tau_{inj}$ increases approximately as $\propto \sigma^{1/2}$.

Better agreement between the simple model and the PIC simulations can be reached by considering the time-dependent acceleration rate $\alpha(t)$. As the magnetic reconnection saturates, the acceleration rate decreases. Figure 11(c) shows the solution that uses the time-dependent acceleration rate $\alpha(t)$ in Figure 6(d) using a stochastic integration technique described by Guo et al. (2010). The final spectral index is about $p = 1.25$, similar to that from the PIC simulation shown in Figure 7(a).

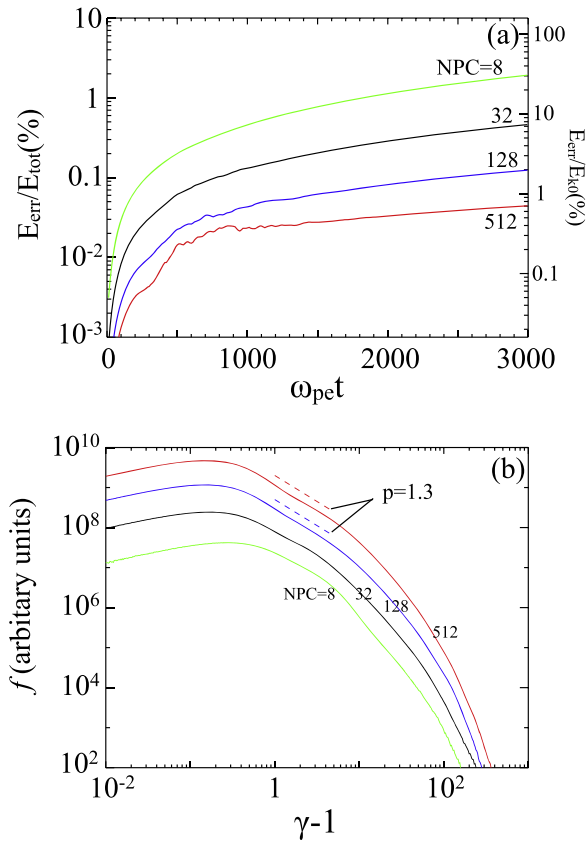


Figure 12. Several cases with $kT_0 = 0.36m_e c^2$ with grid number 2048×2048 , Courant number $C_r = 0.7$ but different numbers of particles per cell from 8 to 512.

5. IMPLICATIONS

We discuss the implication of the above conclusions for understanding the role of magnetic reconnection in magnetically dominated astrophysical systems. Based on the current understanding of magnetic reconnection, multiple X-line reconnection develops when the secondary tearing instability is active in a large-scale collisionless plasma system. This process may also be important when a hierarchy of collisional plasmoids (Loureiro et al. 2007; Bhattacharjee et al. 2009; Uzdensky et al. 2010) develops kinetic-scale current layers that may trigger collisionless reconnection (Daughton et al. 2009; Ji & Daughton 2011). Therefore the collisionless reconnection process discussed here is relevant to a range of high-energy astrophysical problems listed below (see Ji & Daughton 2011, for a comprehensive summary of astrophysical problems with relevant physics).

5.1. PWN

In PWN models, magnetic reconnection has been proposed as a mechanism for dissipating magnetic energy in Poynting-flux-dominated flows (Coroniti 1990; Lyubarsky & Kirk 2001; Kirk & Skjæraasen 2003; Porth et al. 2013) and accelerating particles to high energies (Kirk 2004). In PWNe, the emission flux usually has spectral indices $\alpha_\nu = 0-0.3$ in the radio range, which requires an electron energy distribution $dN/d\gamma \propto \gamma^{-p}$ with $p = 1-1.6$ ($p = 2\alpha_\nu + 1$), too hard to be explained by diffusive shock acceleration (Atoyan 1999). The recently detected >100 MeV Crab flares have photon energies well

above the usually employed upper limit for synchrotron emissions, challenging the traditional acceleration theory (Abdo et al. 2011; Tavani et al. 2011; Bühler & Blandford 2014). There are two main possibilities for explaining the photon energies: (1) a relativistic Doppler boosting of the emitting region (Clausen-Brown & Lyutikov 2012) and/or (2) a strong particle acceleration in a nonideal electric field where $E > B_\perp$, where B_\perp is the magnetic field perpendicular to the particle velocity (Cerutti et al. 2013; M. Lyutikov et al. 2014, in preparation).

These observations suggest that relativistic magnetic reconnection may occur in the Crab Nebula. The power law index revealed in this study is $p = 1-2$, consistent with the inferred spectra in the radio range (Atoyan 1999) and in high energy during the Crab γ -ray flares (Tavani et al. 2011). Explaining these observations requires a fast and efficient dissipation mechanism that converts a substantial fraction of magnetic energy into relativistic particles (Lyutikov et al. 2014). In the Crab pulsar, magnetic reconnection is estimated to be in the plasmoid-dominated regime and can dissipate a nontrivial fraction of the pulsar spin-down power (Uzdensky & Spitkovsky 2014). Our simulations have shown that for a magnetically dominated reconnection layer with $\sigma \gg 1$, the magnetic reconnection rate is greatly enhanced by about one order of magnitude compared to the nonrelativistic limit (see also Liu et al. 2015) and a large fraction of magnetic energy in the system is converted into a nonthermal energy distribution, suggesting an efficient magnetic dissipation and strong nonthermal radiation processes in the Crab wind. The maximum particle energy increases linearly and can be well predicted by assuming particles moving along the reconnecting electric field at the speed of light. There are also relativistic inflow and outflow structures ($\Gamma_{\text{max}} \gtrsim 10$) associated with reconnection, which may boost the emission photon energy and help to explain the observed Crab flares (Clausen-Brown & Lyutikov 2012). It is interesting to note that the reconnection acceleration may also explain the pulsed γ -ray emission, although observations at higher energies are required to further constrain the model (Mochol & Pétri 2015).

5.2. AGN Jets

In AGN jets, a number of γ -ray sources have flat radio spectra with indices around $\alpha_\nu = 0$, meaning the electron energy distribution index may be close to $p = 1$ (Abdo et al. 2010; Hayashida et al. 2015). Several blazars have shown extremely fast variability in the TeV range of the order of several minutes (Aharonian et al. 2007; Albert et al. 2007). Hard power laws $p \sim 1$ in the TeV range have been inferred after removing the effect of the extragalactic background light using various models (Aharonian et al. 2006; Krennrich et al. 2008). For GeV–TeV flat spectrum radio quasars (FSRQ), high radiation efficiency is reported (Zhang et al. 2013) and the electron σ_e , which is measured as magnetic energy power to the electron energy power, is very high—up to the order of 100 (Zhang et al. 2014).

Explaining the fast variability requires the relativistic beaming effect possibly arising from relativistic reconnection outflows (Giannios et al. 2009; Deng et al. 2015). Our kinetic simulations have shown that the Lorentz factor of the maximum outflow speed $\Gamma_x \sim 10$ for $\sigma \sim 1000$. The simulation results and theoretical model predict a hard particle energy distribution consistent with the hard radio spectra observed in

some AGNs (Romanova & Lovelace 1992). Recent advanced AGN emission models have inferred that at least for some types of blazars, particularly FSRQ, strong particle acceleration and/or strong magnetic field is necessary to explain fast flares, and σ inferred from the model fitting can significantly exceed unity, $\sigma \gg 1$ (Chen et al. 2014). Magnetic reconnection may offer an explanation for the simultaneous decrease of magnetic field and increase in emission during the flare phase of blazar flares and is a promising scenario for modeling AGN emissions (Zhang et al. 2014).

5.3. GRBs

In GRBs, the traditional internal-shock model of prompt emission is difficult to reconcile with observations (see Zhang & Yan 2011, and references therein). Magnetic reconnection and associated particle acceleration have been proposed as a key process in GRB models such as the ICMART model (Zhang & Yan 2011) and reconnection-switch model (McKinney & Uzdensky 2012). The efficient magnetic dissipation and particle acceleration during reconnection may be important to understand the emission mechanism in GRBs (Kumar 1999; Spruit et al. 2001; Drenkhahn & Spruit 2002). Gruber et al. (2014) have shown a series of features in GRB prompt emission that are not consistent with the simple synchrotron shock model. For example, the hard low-energy spectra, where the particle energy spectral index is close to $p = 1$ assuming synchrotron radiation (Ghisellini et al. 2000; Preece et al. 2002), and the thermal emission component predicted in the fireball-internal-shock model has rarely been seen in GRBs (Abdo et al. 2009; Zhang & Pe'er 2009).

From our simulation results and analytical model, the particle energy spectral index is close to $p = 1$, consistent with low-energy photon spectra observed in most GRBs (Band et al. 1993; Preece et al. 2000; Gruber et al. 2014). The acceleration in reconnection layers is much faster than the radiation cooling and can maintain the hard spectrum. Using PIC simulation, Spitkovsky (2008) found that in the downstream region of highly relativistic shocks the number of particles in the nonthermal tail is $\sim 1\%$ of the entire downstream population, and they carry 10% of the kinetic energy in the downstream region. In our simulations of relativistic reconnection, the number of nonthermal relativistic particles is $\sim 25\%$ of the total number of particles in the simulation and they carry $\sim 95\%$ of the kinetic energy in the system, meaning relativistic reconnection is much more efficient in producing nonthermal relativistic particles. This efficient conversion from magnetic energy into kinetic energy of nonthermal particles may help solve the efficiency problem in GRB models (Zhang et al. 2007; Deng et al. 2015).

5.4. Nonrelativistic Reconnection Sites

While the primary focus of this paper is relativistic magnetic reconnection, the physics of Fermi acceleration and the formation of a power-law distribution is also applicable to the nonrelativistic regimes previously discussed (Drake et al. 2006, 2010, 2013). Based on our analytical model, the power-law distribution forms only when $\alpha\tau_{\text{inj}} > 1$. The results in this paper demonstrate that this condition is more easily achieved in regimes with $\sigma \gg 1$, but it may also occur with $\sigma < 1$ in sufficiently large reconnection layers. In several preliminary simulations, we have observed the formation of

similar power laws in nonrelativistic proton-electron plasma and will report elsewhere.

X-ray observations of solar flares have shown strong particle acceleration and energy conversion during magnetic reconnection, and the particle distribution often takes power-law distributions, requiring a particle acceleration mechanism that is dominated by nonthermal acceleration (Krucker et al. 2008, 2010; Krucker & Battaglia 2014). As we have shown here, in magnetically dominated regimes, a large fraction of magnetic energy can be converted into particles in a power-law distribution. A similar process is likely to occur in solar flares, where the plasma $\beta = 8\pi nkT/B^2 \sim 0.001\text{--}0.01$ ($\sigma < 1$). However, physics such as the influence of m_i/m_e , strong trapping in the X-line region, and particle escape from the system need to be investigated further (Egedal & Daughton 2015, in preparation).

6. DISCUSSION AND CONCLUSION

The dissipation of magnetic field and particle energization in magnetically dominated systems is of strong interest in high-energy astrophysics. In this study, we use 2D and 3D fully kinetic simulations that resolve the full range of plasma physics to investigate the particle acceleration and plasma dynamics during collisionless magnetic reconnection in a pair plasma with magnetization parameter σ varying from 0.25 to 1600. A force-free current layer, which does not require a hot plasma population in the current layer, is implemented as the initial condition.

We find that the evolution of the current sheet and acceleration of particles has two stages. In the early stage, an extended reconnection region forms and generates a parallel electric field that accelerates particles in the current layer. As time proceeds, the layer breaks into multiple plasmoids (flux ropes in 3D) due to the secondary tearing instability. The motional electric field in the reconnection layer strongly accelerates energetic particles via a first-order relativistic Fermi process leading to the conversion of most of the free energy in the system. A large fraction of the magnetic energy is quickly converted into the kinetic energy of nonthermal relativistic particles (within a few light-crossing times) and the eventual energy spectra show a power law $f \propto (\gamma - 1)^{-p}$, with the spectral index p decreasing with σ and system size and approaching $p = 1$. The formation of the power-law distribution can be described by a simple model that includes both inflow and the Fermi acceleration. This model also appears to explain recent PIC simulations (Melzani et al. 2014b; Sironi & Spitkovsky 2014; Werner et al. 2014), which reported hard power-law distributions after subtracting the initial hot plasma population inside the current layer. For the more realistic limit with both particle loss and injection, the spectral index $p = 1 + 1/(\alpha\tau_{\text{esc}})$, recovering the classical Fermi solution. If the escape is caused by convection out of the reconnection region $\tau_{\text{esc}} = L_x/V_x$, the spectral index should approach $p = 1$ when $\alpha\tau_{\text{esc}} \gg 1$ in the high- σ regime. In preliminary 2D simulations using open boundary conditions, we have confirmed this trend and will report elsewhere. For the nonrelativistic limit, the reconnection needs to be sustained over a longer time to form a power law.

We have also shown that in sufficiently high- σ regimes the magnetic reconnection rate is enhanced and relativistic inflow and outflow structures develop. The scaling follows the prediction based on the Lorentz contraction of plasma passing

Table 2
List of Simulation Runs Used to Test Numerical Convergence

Run	$kT_0/m_e c^2$	Grid Numbers	Time Step (C_r)	NPC	$E_{\text{err}}/E_{\text{total}}$	E_{err}/E_{k0}
A-1	0.36	4096×4096	0.9	2	10%	159%
A-2	0.36	4096×4096	0.9	8	2.4%	38%
A-3	0.36	4096×4096	0.9	32	0.56%	9%
A-4	0.36	4096×4096	0.9	128	0.084%	1.3%
A-5	0.36	2048×2048	0.9	8	5%	80%
A-6	0.36	2048×2048	0.9	32	1.2%	20%
A-7	0.36	2048×2048	0.9	128	0.3%	5%
A-8	0.36	2048×2048	0.7	8	1.9%	30%
A-9	0.36	2048×2048	0.7	32	0.45%	7%
A-10	0.36	2048×2048	0.7	128	0.12%	1.9%
A-11	0.36	2048×2048	0.7	512	0.04%	0.6%
A-12	0.36	2048×2048	0.5	8	0.75%	12%
A-13	0.36	2048×2048	0.5	32	0.19%	3%
A-14	0.36	2048×2048	0.5	128	0.05%	0.8%
B-1	0.09	4096×4096	0.9	2	9%	474%
B-2	0.09	4096×4096	0.9	8	1.9%	100%
B-3	0.09	4096×4096	0.9	32	0.42%	22%
B-4	0.09	4096×4096	0.9	128	0.05%	2.6%
B-5	0.09	2048×2048	0.9	8	4.2%	212%
B-6	0.09	2048×2048	0.9	32	0.9%	45%
B-7	0.09	2048×2048	0.9	128	0.24%	12%
B-8	0.09	2048×2048	0.7	8	1.6%	80%
B-9	0.09	2048×2048	0.7	32	0.37%	19%
B-10	0.09	2048×2048	0.7	128	0.1%	5%
B-11	0.09	2048×2048	0.5	8	0.6%	30%
B-12	0.09	2048×2048	0.5	32	0.13%	7%
B-13	0.09	2048×2048	0.5	128	0.04%	2%
C-1	0.01	4096×4096	0.9	2	8.5%	3000%
C-2	0.01	4096×4096	0.9	8	1.7%	595%
C-3	0.01	4096×4096	0.9	32	0.36%	126%
C-4	0.01	4096×4096	0.9	128	0.09%	32%
C-5	0.01	4096×4096	0.9	512	0.03%	10%
C-6	0.01	2048×2048	0.9	32	0.75%	265%
C-7	0.01	2048×2048	0.9	128	0.19%	67%
C-8	0.01	2048×2048	0.9	512	0.08%	29%
C-9	0.01	2048×2048	0.7	32	0.28%	102%
C-10	0.01	2048×2048	0.7	128	0.08%	28%
C-11	0.01	2048×2048	0.7	512	0.044%	15%
C-12	0.01	2048×2048	0.5	32	0.11%	39%
C-13	0.01	2048×2048	0.5	128	0.035%	12%
C-14	0.01	2048×2048	0.5	512	0.014%	5%

Note. All the runs are for $\sigma = 25$ and $L_x \times L_z = 600d_i \times 388d_i$ and were performed over a duration $\omega_{pe}t = 3000$. Note $kT_0/m_e c^2$ is the initial plasma temperature normalized by rest energy $m_e c^2$. Time step is represented by the dimensionless Courant number $C_r = c\Delta t/\Delta r$, where $\Delta r = \Delta x\Delta y\Delta z/(\Delta x\Delta y + \Delta y\Delta z + \Delta x\Delta z)$. NPC represents the number of particle pairs per cell. $E_{\text{err}}/E_{\text{total}}$ represents the ratio between change of total energy and the initial total energy. E_{err}/E_{k0} represents the ratio between change of total energy and the initial plasma kinetic energy.

through the diffusion region. Although 3D magnetic turbulence is generated as a consequence of the growth of the secondary tearing instability and kink instability, the particle acceleration, energy release, and reconnection rate in the 3D simulation are comparable to the corresponding 2D simulation.

Our study has demonstrated that relativistic magnetic reconnection is a highly efficient energy-dissipation mechanism in the magnetically dominated regimes. The plasma distribution in the reconnection layer features power-law

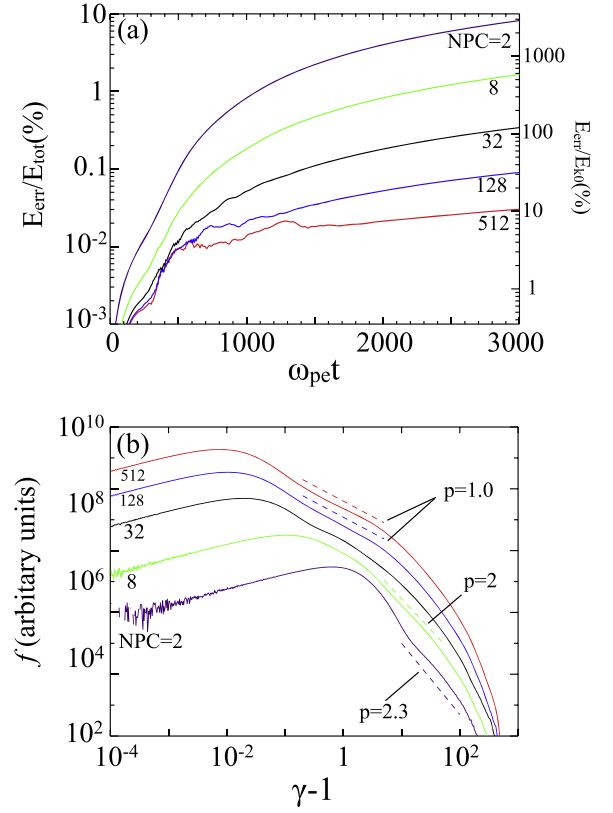


Figure 13. Several cases for $kT_0 = 0.01m_e c^2$ with grid number 4096×4096 and $C_r = 0.9$ but different numbers of particles per cell from 2 to 512.

energy spectra, which may be important in understanding the nonthermal emissions from objects like pulsars, jets from black holes, and GRBs. Both the inflow and outflow speeds approach the speed of light and have Lorentz factors of a few, which may explain the fast variability and high luminosity observed in those high-energy astrophysical systems. These findings on particle acceleration and plasma dynamics during relativistic reconnection substantiate the important role of magnetic reconnection in high-energy astrophysical systems.

We gratefully acknowledge useful discussions with and comments from Andrey Beresnyak, Xuhui Chen, Wei Cui, Wei Deng, Brenda Dingus, Jim Drake, Joe Giacalone, Dimitrios Giannios, Serguei Komissarov, Pawan Kumar, Xiaocan Li, Maxim Lyutikov, Rob Preece, Marc Swisdak, Alexander Tchekhovskoy, Dmitri Uzdensky, Yajie Yuan, Gary Zank, Bing Zhang, and Haocheng Zhang. This work is supported by the DOE through the LDRD program at LANL and DOE/OFES support to LANL in collaboration with CMSO, and by NASA through the Heliospheric Theory Program. The research is part of the Blue Waters sustained-petascale computing project, which is supported by the NSF (Grant No. OCI 07-25070) and the state of Illinois. Additional simulations were performed at the National Center for Computational Sciences at ORNL and with LANL institutional computing.

APPENDIX NUMERICAL CONVERGENCE

The accuracy of PIC kinetic simulations depends on a series of numerical parameters such as cell size, time step, and the

number of macro-particles per cell (e.g., Birdsall & Langdon 1991). The numerical convergence of simulation results has rarely been explicitly checked when modeling astrophysical problems using PIC simulations, and often a small number of macro-particles are used. Here we examine the numerical convergence of our results on these numerical parameters using VPIC code for different initial temperatures from $kT_0 = 0.01$ to $0.36 m_e c^2$. Our test case has $\sigma = 25$ with box size $L_x \times L_z = 600d_i \times 388d_i$ and simulation time $\omega_{pe} t = 3000$. We find that numerical heating can become unacceptably large when a small number of particles per cell is used. In Table 2 we list the key parameters for the test. Although for most cases the violation in energy conservation is small ($E_{\text{err}}/E_{\text{tot}}$ within 1%), the numerical heating can significantly modify the particle distribution since the initial kinetic energy is a small fraction of the total energy. Therefore to obtain trustworthy results that are numerically converged, the violation of energy conservation should be much less than the initial kinetic energy $E_{\text{err}}/E_{k0} \ll 1$. Figure 12 shows several cases with $kT_0 = 0.36 m_e c^2$ with grid number 2048×2048 , Courant number $C_r = 0.7$, and different numbers of particles per cell from 8 to 512. Figure 13 shows several cases for $kT_0 = 0.01 m_e c^2$ with grid number 4096×4096 and $C_r = 0.9$ but different numbers of particles per cell from 2 to 512. Both figures show that as the total energy change in the numerical simulations becomes smaller than the initial kinetic energy $E_{\text{err}}/E_{k0} \ll 1$, the numerical heating has a negligible effect on the distribution function.

REFERENCES

- Abdo, A. A., Ackermann, M., Arimoto, M., et al. 2009, *Sci*, **323**, 1688
- Abdo, A. A., Ackermann, M., Agudo, I., et al. 2010, *ApJ*, **716**, 30
- Abdo, A. A., Ackermann, M., Ajello, M., et al. 2011, *Sci*, **331**, 739
- Achterberg, A., Gallant, Y. A., Kirk, J. G., & Guthmann, A. W. 2001, *MNRAS*, **328**, 393
- Aharonian, F., Akhperjanian, A. G., Bazer-Bachi, A. R., et al. 2007, *ApJL*, **664**, L71
- Aharonian, F., Akhperjanian, A. G., Bazer-Bachi, A. R., et al. 2006, *Natur*, **440**, 1018
- Albert, J., Aliu, E., Anderhub, H., et al. 2007, *ApJ*, **669**, 862
- Arons, J. 2012, *SSRv*, **173**, 341
- Atayan, A. M. 1999, *A&A*, **346**, L49
- Band, D., Matteson, J., Ford, L., et al. 1993, *ApJ*, **413**, 281
- Bessho, N., & Bhattacharjee, A. 2012, *ApJ*, **750**, 129
- Bhattacharjee, A., Huang, Y.-M., Yang, H., & Rogers, B. 2009, *PhPI*, **16**, 112102
- Birdsall, C. K., & Langdon, A. B. 1991, in *Plasma Physics via Computer Simulation* (New York: Taylor & Francis)
- Birn, J., Drake, J. F., Shay, M. A., et al. 2001, *JGR*, **106**, 3715
- Blackman, E. G., & Field, G. B. 1994, *PhRvL*, **72**, 494
- Blandford, R., & Eichler, D. 1987, *PhR*, **154**, 1
- Bowers, K. J., Albright, B. J., Yin, L., et al. 2009, *JPhCS*, **180**, 012055
- Bühler, R., & Blandford, R. 2014, *RPPH*, **77**, 066901
- Celotti, A., & Ghisellini, G. 2008, *MNRAS*, **385**, 283
- Cerutti, B., Uzdensky, D. A., & Begelman, M. C. 2012, *ApJ*, **746**, 148
- Cerutti, B., Werner, G. R., Uzdensky, D. A., & Begelman, M. C. 2013, *ApJ*, **770**, 147
- Che, H., Drake, J. F., & Swisdak, M. 2011, *Natur*, **474**, 184
- Chen, X., Chatterjee, R., Zhang, H., et al. 2014, *MNRAS*, **441**, 2188
- Clausen-Brown, E., & Lyutikov, M. 2012, *MNRAS*, **426**, 1374
- Comisso, L., & Asenjo, F. A. 2014, *PhRvL*, **113**, 045001
- Coroniti, F. V. 1990, *ApJ*, **349**, 538
- Dahlin, J. T., Drake, J. F., & Swisdak, M. 2014, *PhPI*, **21**, 092304
- Daughton, W. 1999, *PhPI*, **6**, 1329
- Daughton, W., & Karimabadi, H. 2007, *PhPI*, **14**, 072303
- Daughton, W., Nakamura, T. K. M., Karimabadi, H., Roytershteyn, V., & Loring, B. 2014, *PhPI*, **21**, 052307
- Daughton, W., Roytershteyn, V., Albright, B. J., et al. 2009, *PhRvL*, **103**, 065004
- Daughton, W., Roytershteyn, V., Karimabadi, H., et al. 2011, *NatPh*, **7**, 539
- Daughton, W., Scudder, J., & Karimabadi, H. 2006, *PhPI*, **13**, 072101
- de Gouveia dal Pino, E. M., & Lazarian, A. 2005, *A&A*, **441**, 845
- Deng, W., Li, H., Zhang, B., & Li, S. 2015, *ApJ*, **805**, 163
- Drake, J. F., Opher, M., Swisdak, M., & Chamoun, J. N. 2010, *ApJ*, **709**, 963
- Drake, J. F., Shay, M. A., Thongthai, W., & Swisdak, M. 2005, *PhRvL*, **94**, 095001
- Drake, J. F., Swisdak, M., Che, H., & Shay, M. A. 2006, *Natur*, **443**, 553
- Drake, J. F., Swisdak, M., & Fermo, R. 2013, *ApJL*, **763**, L5
- Drenkhahn, G., & Spruit, H. C. 2002, *A&A*, **391**, 1141
- Drury, L. O. 2012, *MNRAS*, **422**, 2474
- Egedal, J., Daughton, W., Le, A., & Borg, A. L. 2015, arXiv:1504.08045
- Fu, X. R., Lu, Q. M., & Wang, S. 2006, *PhPI*, **13**, 012309
- Galsgaard, K., Titov, V. S., & Neukirch, T. 2003, *ApJ*, **595**, 506
- Ghisellini, G., Celotti, A., & Lazzati, D. 2000, *MNRAS*, **313**, L1
- Giannios, D., Uzdensky, D. A., & Begelman, M. C. 2009, *MNRAS*, **395**, L29
- Gruber, D., Goldstein, A., Weller von Ahlefeld, V., et al. 2014, *ApJS*, **211**, 12
- Guo, F., Jokipii, J. R., & Kota, J. 2010, *ApJ*, **725**, 128
- Guo, F., Li, H., Daughton, W., & Liu, Y.-H. 2014, *PhRvL*, **113**, 155005
- Hayashida, M., Nalewajko, K., Madejski, G. M., et al. 2015, arXiv:1502.04699
- Hoshino, M. 2012, *PhRvL*, **108**, 135003
- Huang, C., Lu, Q., & Wang, S. 2010, *PhPI*, **17**, 072306
- Ji, H., & Daughton, W. 2011, *PhPI*, **18**, 111207
- Kirk, J. G. 2004, *PhRvL*, **92**, 181101
- Kirk, J. G., & Skjæraasen, O. 2003, *ApJ*, **591**, 366
- Kowal, G., de Gouveia Dal Pino, E. M., & Lazarian, A. 2011, *ApJ*, **735**, 102
- Kowal, G., de Gouveia Dal Pino, E. M., & Lazarian, A. 2012, *PhRvL*, **108**, 241102
- Krennrich, F., Dwek, E., & Imran, A. 2008, *ApJL*, **689**, L93
- Krucker, S., & Battaglia, M. 2014, *ApJ*, **780**, 107
- Krucker, S., Hudson, H. S., Glesener, L., et al. 2010, *ApJ*, **714**, 1108
- Krucker, S., Battaglia, M., Cargill, P. J., et al. 2008, *A&ARv*, **16**, 155
- Kulsrud, R. M. 1998, *PhPI*, **5**, 1599
- Kumar, P. 1999, *ApJL*, **523**, L113
- Larrabee, D. A., Lovelace, R. V. E., & Romanova, M. M. 2003, *ApJ*, **586**, 72
- Lazarian, A., & Opher, M. 2009, *ApJ*, **703**, 8
- Litvinenko, Y. E. 1999, *A&A*, **349**, 685
- Liu, W., Li, H., Yin, L., et al. 2011, *PhPI*, **18**, 052105
- Liu, Y.-H., Daughton, W., Karimabadi, H., Li, H., & Peter Gary, S. 2014, *PhPI*, **21**, 022113
- Liu, Y.-H., Daughton, W., Karimabadi, H., Li, H., & Roytershteyn, V. 2013, *PhRvL*, **110**, 265004
- Liu, Y.-H., Guo, F., Daughton, W., Li, H., & Hesse, M. 2015, *PhRvL*, **114**, 095002
- Longair, M. S. 1994, in *High Energy Astrophysics, Vol 2, Stars, the Galaxy and the Interstellar Medium* (Cambridge, UK: Cambridge Univ. Press)
- Loureiro, N. F., Schekochihin, A. A., & Cowley, S. C. 2007, *PhPI*, **14**, 100703
- Lyubarsky, Y., & Kirk, J. G. 2001, *ApJ*, **547**, 437
- Lyubarsky, Y. E. 2005, *MNRAS*, **358**, 113
- Lyutikov, M., & Uzdensky, D. 2003, *ApJ*, **589**, 893
- McKinney, J. C., & Uzdensky, D. A. 2012, *MNRAS*, **419**, 573
- Melzani, M., Walder, R., Folini, D., Winisdoerffer, C., & Favre, J. M. 2014a, *A&A*, **570**, A111
- Melzani, M., Walder, R., Folini, D., Winisdoerffer, C., & Favre, J. M. 2014b, *A&A*, **570**, A112
- Mochol, I., & Pétri, J. 2015, *MNRAS*, **449**, L51
- Oka, M., Phan, T.-D., Krucker, S., Fujimoto, M., & Shinohara, I. 2010, *ApJ*, **714**, 915
- Porth, O., Komissarov, S. S., & Keppens, R. 2013, *MNRAS*, **431**, L48
- Preece, R. D., Briggs, M. S., Giblin, T. W., et al. 2002, *ApJ*, **581**, 1248
- Preece, R. D., Briggs, M. S., Mallozzi, R. S., et al. 2000, *ApJS*, **126**, 19
- Priest, E., & Forbes, T. 2000, *Magnetic Reconnection* (Cambridge, UK: Cambridge Univ. Press)
- Pritchett, P. L. 2006, *JGRA*, **111**, 10212
- Romanova, M. M., & Lovelace, R. V. E. 1992, *A&A*, **262**, 26
- Sironi, L., & Spitkovsky, A. 2014, *ApJL*, **783**, L21
- Spitkovsky, A. 2008, *ApJL*, **682**, L5
- Spruit, H. C., Daigne, F., & Drenkhahn, G. 2001, *A&A*, **369**, 694
- Takamoto, M. 2013, *ApJ*, **775**, 50
- Tavani, M., Bulgarelli, A., Vittorini, V., et al. 2011, *Sci*, **331**, 736
- Thompson, C. 1994, *MNRAS*, **270**, 480
- Titov, V. S., Galsgaard, K., & Neukirch, T. 2003, *ApJ*, **582**, 1172
- Uzdensky, D. A., Loureiro, N. F., & Schekochihin, A. A. 2010, *PhRvL*, **105**, 235002
- Uzdensky, D. A., & Spitkovsky, A. 2014, *ApJ*, **780**, 3

- Werner, G. R., Uzdensky, D. A., Cerutti, B., Nalewajko, K., & Begelman, M. C. 2014, arXiv:1409.8262
- Yin, L., Daughton, W., Karimabadi, H., et al. 2008, *PhRvL*, **101**, 125001
- Zank, G. P., Le Roux, J. A., Webb, G. M., Dosch, A., & Khabarov, O. 2014, *ApJ*, **797**, 28
- Zenitani, S., Hesse, M., & Klimas, A. 2009, *ApJ*, **696**, 1385
- Zenitani, S., & Hoshino, M. 2001, *ApJL*, **562**, L63
- Zenitani, S., & Hoshino, M. 2005, *PhRvL*, **95**, 095001
- Zenitani, S., & Hoshino, M. 2007, *ApJ*, **670**, 702
- Zenitani, S., & Hoshino, M. 2008, *ApJ*, **677**, 530
- Zhang, B., & Pe'er, A. 2009, *ApJL*, **700**, L65
- Zhang, B., & Yan, H. 2011, *ApJ*, **726**, 90
- Zhang, B., Liang, E., Page, K. L., et al. 2007, *ApJ*, **655**, 989
- Zhang, H., Xuhui Chen, Markus Bottcher, Fan Guo, & Hui Li 2015, *ApJ*, **804**, 58
- Zhang, J., Liang, E.-W., Sun, X.-N., et al. 2013, *ApJL*, **774**, L5